AGU PUBLICATIONS

Water Resources Research

RESEARCH ARTICLE
10.1002/2013WR014020

Key Points:
- Inversion of nonlinear groundwater model
- To perform quantitative hydrogeophysics
- To develop a methodology to characterize seawater intrusion

Correspondence to:
J. Beaujean,
jean.beaujean@gmail.com

Citation:
Beaujean, J., F. Nguyen, A. Kemna, A. Antonsson, and P. Engesgaard (2014), Calibration of seawater intrusion models: Inverse parameter estimation using surface electrical resistivity tomography and borehole data, *Water Resour. Res.*, *50*, 6828–6849, doi:10.1002/2013WR014020.

Received 17 JUN 2013
Accepted 1 AUG 2014
Accepted article online 5 AUG 2014
Published online 22 AUG 2014

Calibration of seawater intrusion models: Inverse parameter estimation using surface electrical resistivity tomography and borehole data

J. Beaujean[1], F. Nguyen[1,2], A. Kemna[3], A. Antonsson[4], and P. Engesgaard[4]

[1]Department of Architecture, Geology, Environment and Construction, University of Liège, Liège, Belgium, [2]Agrosphere, IBG-3 (formerly ICG-4), Forschungszentrum Juelich GmbH, Juelich, Germany, [3]Department of Geodynamics and Geophysics, University of Bonn, Bonn, Germany, [4]Department of Geosciences and Natural Resource Management, University of Copenhagen, Copenhagen, Denmark

Abstract Electrical resistivity tomography (ERT) can be used to constrain seawater intrusion models because of its high sensitivity to total dissolved solid contents (TDS) in groundwater and its relatively high lateral coverage. However, the spatial variability of resolution in electrical imaging may prevent the correct recovery of the desired hydrochemical properties such as salt mass fraction. This paper presents a sequential approach to evaluate the feasibility of identifying hydraulic conductivity and dispersivity in density-dependent flow and transport models from surface ERT-derived mass fraction. In the course of this study, geophysical inversion was performed by using a smoothness constraint Tikhonov approach, whereas the hydrological inversion was performed using a gradient-based Levenberg-Marquardt algorithm. Two synthetic benchmarks were tested. They represent a pumping experiment in a homogeneous and heterogeneous coastal aquifer, respectively. These simulations demonstrated that only the lower salt mass fraction of the seawater-freshwater transition zone can be recovered for different times. This ability has here been quantified in terms of cumulative sensitivity and our study has further demonstrated that the mismatch between the targeted and the recovered salt mass fraction occurs from a certain threshold. We were additionally able to explore the capability of sensitivity-filtered ERT images using ground surface data only to recover (in both synthetic cases) the hydraulic conductivity while the dispersivity is more difficult to estimate. We attribute the latter mainly to the lack of ERT-derived data at depth (where resolution is poorer) as well as to the smoothing effect of the ERT inversion.

1. Introduction

Along coastal regions, groundwater quality and coastal ecosystems are threatened by excessive groundwater withdrawals, sea level rise, and storm events [e.g., *Bear et al*., 1999; *Michael et al*., 2005; *Vandenbohede et al*., 2010; *Werner et al*., 2012]. To study the occurrence of seawater intrusion and to investigate groundwater resources management problems, a combination of robust measuring technologies and reliable predictions based on numerical models are necessary.

One key aspect in the calibration of seawater intrusion (SWI) models involves reproducing measured chloride concentrations or TDS in groundwater [e.g., *Bear et al*., 1999; *Cheng and Ouazar*, 2004], a key diagnostic of seawater contamination. In arid and semiarid environments, chloride has the advantages of being one of the major anions in seawater, chemically stable, and a suitable tracer that moves at the same rate as intruding seawater [*Gupta*, 2010]. The most important hydraulic parameters in SWI models are hydraulic conductivity and dispersivity [*Shoemaker*, 2004; *Sanz and Voss*, 2006]. The hydraulic conductivity of an aquifer can be estimated based on either field-scale or laboratory tests. Dispersivity values are usually estimated by tracer tests [e.g., *Mallants et al*., 1999] or, more commonly, by modeling the observed distributions of seawater. The anisotropy ratio of hydraulic parameters also plays a significant role in SWI modeling. This is a key characteristic of real aquifers, affecting the steepness of the interface (i.e., the SWI toe and the flux of seawater that enters the aquifer through the seaside boundary), while the longitudinal and transversal dispersion control the width of the mixing zone [*Abarca*, 2006]. Dispersion generates a transition zone across which the concentration of salt varies between freshwater and seawater. Vertical transversal dispersion is

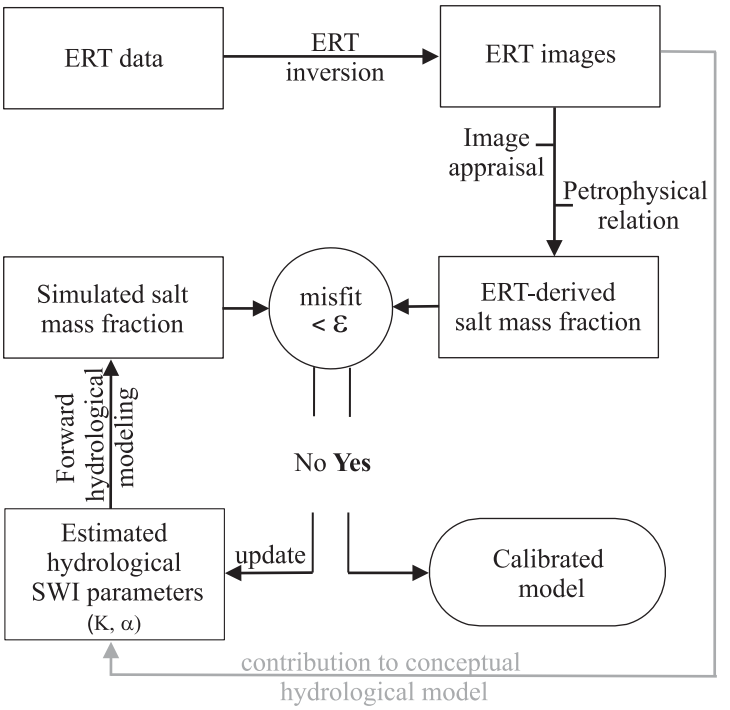

Figure 1. Flowchart of SWI model calibration using geophysical ERT data and a petrophysical relationship linking bulk electrical conductivity to salt mass fraction. The hydrogeophysical inversion methodology consists of two separate steps (so-called uncoupled approach): (1) ERT inversion to determine the bulk electrical conductivity distribution, which is filtered using an image appraisal tool and (2) inverse parameter estimation (calibration loop) is performed to estimate the SWI model parameters using the ERT-derived salt mass fraction data.

the primary mechanism responsible for seawater circulation and is important since it generates the transition zone, indicative of the salinity of pumped water [*Dagan*, 2006]. Salinity generally derives from chloride concentration, and may compromise drinking water standards. In coastal aquifers where continuous overexploitation disturbs the groundwater balance and reduces the freshwater submarine groundwater discharge, groundwater levels are lowered and SWI results in a salinity breakthrough. Both horizontal and vertical transversal dispersion are also important when the freshwater-seawater interface deviates from a conventional interface shape. Other configurations may also result from nonsteady state conditions, dissolution of salt beds, or a larger-scale multiple-aquifer system [e.g., *Yechieli et al*., 2001].

Inverse calibration of coupled flow and transport models started a few decades ago [e.g., *Wagner and Gorelick*, 1987; *Sun et al*., 1995]. More recently, *Carrera et al*. [2005] presented a thorough comparison between existing inverse calibration methods used for general aquifer characterization. Despite the fact that various inversion tools have been developed (e.g., PEST [*Doherty*, 2004] or UCODE [*Poeter et al*., 2005]) there is still a limited body of literature regarding inverse calibration of SWI models [e.g., *Van Meir and Lebbe*, 2005; *Carrera et al*., 2009].

Concentration measurements collected in a well are often spatially scarce and strongly dependent on the heterogeneity of the model [*Hill and Tiedeman*, 2007]. The use of wells is challenging since the location of the seawater intrusion is, a priori, unknown. Moreover, existing wells may present defects, e.g., a well with a corroded casing or screened through multiple geological units with confined and unconfined layers, potentially leading to direct preferential entryways for seawater and hydraulic connection between aquifers zones [*Carrera et al*., 2009; *Herckenrath et al*., 2012]. Concentration measurements are indeed very sensitive to flow within open boreholes [*Shalev et al*., 2009]. While a multiscreen well equipped with sealed screens can be constructed without short-circuiting water, such wells are both expensive and difficult to achieve [*Guhl et al*., 2006; *Ogilvy et al*., 2009].

Geophysical methods constrained with geochemical data have been used for mapping and delineating SWI [e.g., *Nguyen et al*., 2009; *Hermans et al*., 2012]. Water electrical conductivity (EC) varies from $<$500 μS/cm for freshwater to $>$25,000 μS/cm for seawater, making SWI tracking a good target for electrical and electromagnetic methods [*Goldman and Kafri*, 2006]. Currently, geophysical techniques are increasingly being used for hydrological model parameterization and calibration [e.g., *Binley et al*., 2002; *Ferré et al*., 2009; *Herckenrath et al*., 2012]. The most typical approach for integrating hydrogeophysical data is referred to as "uncoupled hydrogeophysical" inversion (Figure 1). This technique involves constraining hydraulic parameters using geophysically derived data and generally first requires a geophysical inversion, in which geophysical

properties (e.g., true resistivity) are converted to hydrological data (e.g., concentration of a contaminant) through a petrophysical relationship. The inverse hydrological calibration is then performed on the inferred hydrological data. *Lebbe* [1999] studied SWI in a shallow shore environment and calibrated a density-dependent flow and solute transport model using head measurements and borehole resistivity logs. This procedure included estimation of flow and solute transport parameters of a numerical model and parameters related to the resistivity-salinity relation. The study illustrated that it was possible to identify horizontal and vertical hydraulic conductivities, longitudinal and transversal dispersivities, and effective porosity in a homogeneous case. In *Compte and Banton* [2007], groundwater and geoelectrical models were cross validated, first by visually comparing field electrical images and simulated chloride concentrations and second by measuring electrical data with synthetic data calculated using a site-specific petrophysical relationship. In *Koukadaki et al*. [2007], the Ghyben-Herzberg approximation was used to calibrate a groundwater model based on hydraulic heads, by converting electrical resistivity to hydraulic conductivity. In this context, geophysical models are related to hydraulic parameters and/or simulated hydrological data through a model equation [*Hill and Tiedeman*, 2007]. Inherent geophysical limitations, such as resolution loss or petrophysical uncertainty are usually not addressed in SWI studies. Whereas the former should be addressed using image appraisal tools, uncertainties in the petrophysical model are more challenging to address [*Day-Lewis et al*., 2005; *Linde et al*., 2006].

Using numerical benchmarks, this paper demonstrates that density-dependent flow and transport models can be calibrated with surface ERT-derived data only if the spatial variability of sensitivity within the geophysical model is taken into account. We also seek to assess an optimal geophysical data collection strategy and to compare different approaches to hydrogeological calibration.

2. Seawater Intrusion Benchmark Models

Geologic systems are not homogeneous or uniform. Nevertheless, benchmark models which are homogeneous allow us to define a reference ideal case on which to test new developments and to assess their limitations. Moreover, within the context of SWI, the toe penetration and the width of the mixing zone are susceptible to reproduction by an "equivalent" homogeneous and anisotropic medium instead of a random heterogeneous porous medium. In the case of large-scale contrasting heterogeneities, for example, at the regional scale, heterogeneity has to be explicitly represented in the models [*Abarca*, 2006]. In this study, we investigate the ability of ERT to calibrate a simple yet insightful and representative homogeneous media, and a more complex dipping structure, which provides a heterogeneous example for realistic geophysical ERT and hydrogeological data acquisition [*Ogilvy et al*., 2009].

2.1. Homogeneous Case

The groundwater model domain has a length of 4389 m and a depth of 61 m (Figure 2a, top), similar to *Huyakorn et al*. [1987]. It is a 2.5-D SWI problem (assuming a 3-D sink such as pumping in a 2-D medium) in a phreatic aquifer subject to pumping from a shallow well, screened in the upper 12 m and placed at 2194 m from the ocean, assumed to be uniformly distributed along the coastline. For that reason, an average value of water withdrawal rate per unit length of the coast was set to 8.6 m^3/d/m and a uniformly distributed recharge of 0.3 m/yr/m is set on the top of the aquifer. This situation is representative of aquifers where shallow coastal well collectors are installed along a line parallel to the coast, as found in Israel, for example [*Bear et al*., 1999].

Freshwater enters the aquifer from the left side, and the coastal side corresponds to the right side. A constant hydraulic head value of 1.5 m was assigned to the left side while an equivalent freshwater head value of 0 m linearly increasing to 1.5 m was assigned to the right (seaward) boundary from the top to the bottom of the aquifer. Dynamic equilibrium and hydrostatic pressure distribution were assumed with stationary seawater. No-flow condition was prescribed to the bottom boundary and flow was assumed parallel to the cross section, neglecting the groundwater flow parallel to the coast in the vicinity of the pumping well (Figure 2a). For solute transport, associated concentrations as scaled salt mass fraction (SMF) were used for both sea and inland boundaries. A prescribed value of 1 was assigned in the deeper part of the aquifer ($-61\ \text{m} < y < -12\ \text{m}$). To allow advective mass transport out of the system, the normal SMF gradient was set equal to zero over the upper part ($-12\ \text{m} < y < 0\ \text{m}$). This leads to realistic concentrations at shallow depths, where freshwater discharge occurs. A scaled SMF of zero was assigned over the entire thickness of

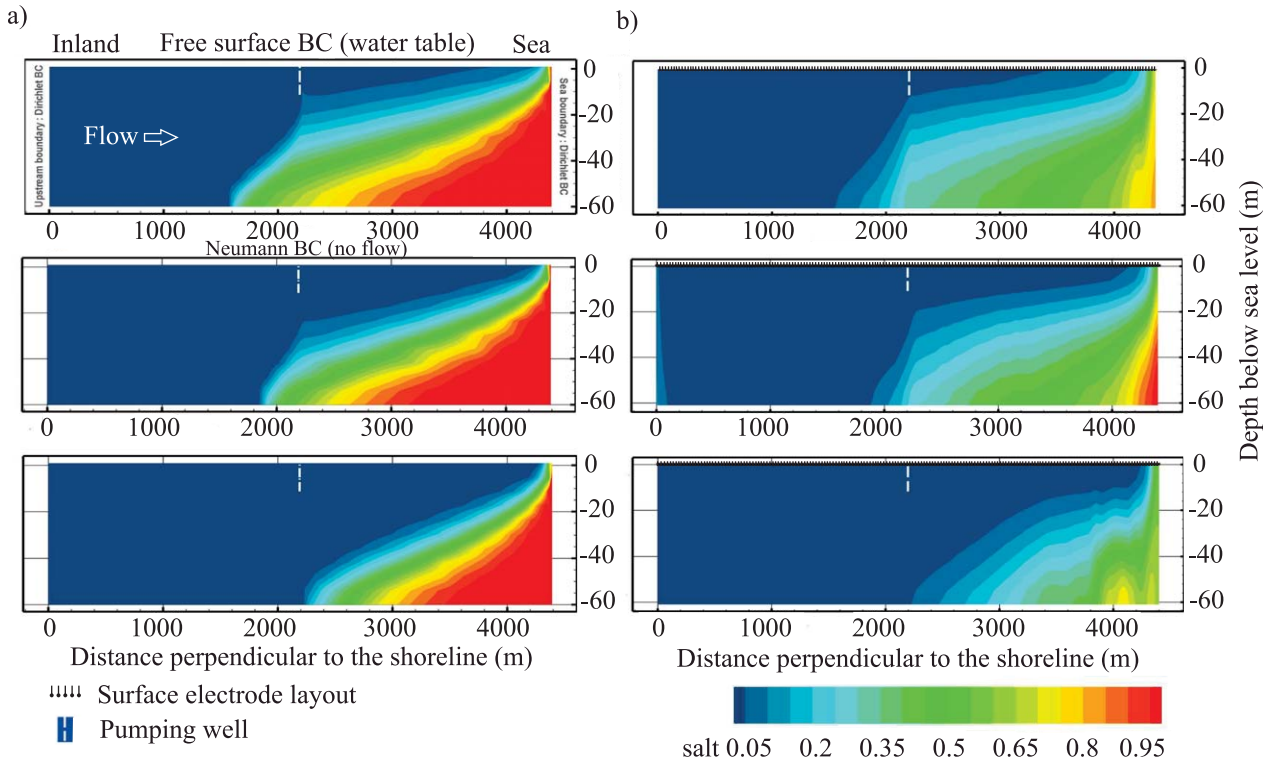

Figure 2. (a) Domain geometry with boundary conditions for the homogeneous SWI model and results of the simulation after 1, 10, and 50 years (from bottom to top). (b) ERT-derived SMF models for the corresponding times.

the aquifer at the inland boundary. Initially, the simulation ran for 50 years with a maximum time step of 5.4 h, thereby avoiding numerical instability due to poor temporal discretization. A time step multiplier was used to control the maximum allowed absolute change of 0.01 (expressed as SMF) in nodal concentration during any time step. As the simulation ended, no changes over time were observed in concentration and hydraulic head or in the intruding part of the seawater wedge. A simulation time of 50 years was necessary to produce an upconing (Figure 2a). Simulations of SWI were performed using the finite element numerical model HydroGeoSphere (HGS) [*Therrien et al.*, 2010]. Here model development was undertaken at the scale of a few kilometers, although SWI investigation can also be undertaken at the scale of tens of meters [e.g., *Van Meir*, 2001]. Altering the scale in this way would result in both a significantly faster hydrodynamics for which our methodological developments would still be applicable.

The 2-D vertical cross-sectional model was discretized with a nodal spacing of 25 m in the longitudinal direction and 6.1 m in vertical direction. This nodal spacing was selected with specific considerations in mind: (1) the Peclet number should be less than 1 to minimize the risk of instability, especially in the portion of the aquifer near the well and the coastal interface; and (2) the mesh matches a uniform corresponding grid used in the geophysical model. The model parameters used in the benchmark simulation are homogeneous horizontal and vertical hydraulic conductivities, $K_h = 7.06 \times 10^{-3}$ m/s and $K_v = 7.06 \times 10^{-4}$ m/s, and longitudinal and transversal dispersivities, $\alpha_L = 45.7$ m and $\alpha_T = 9.1$ m. According to *Huyakorn et al.* [1987], these hydraulic parameters are similar to those found in coastal aquifers in Florida, and the hydraulic conductivity anisotropy ratio is typical of aquifers in interbedded sandstone and carbonate rocks. The chosen dispersivity values are relatively high but not unrealistic. They promote an extensive transition (mixture) zone between freshwater and seawater while avoiding convergence difficulties. Horizontal-to-vertical hydraulic conductivity ratios between 50 and 100 have been used to model many coastal aquifers [*Huyakorn et al.*, 1987; *Pandit et al.*, 1991]. *Dagan* [2006] calculated a ratio of 10 for dispersivity in sandy coastal aquifers whereas values up to 10 to 100 were used in other studies [e.g., *Abarca*, 2006; *Herckenrath et al.*, 2012].

Bulk electrical conductivity values σ_b (μS/cm; or its inverse, bulk resistivity ρ_b (Ω m)) were computed from scaled SMF and water electrical conductivity, σ_w (μS/cm), through a transformation similar to equation (11)

in *Nguyen et al*. [2009]. Here σ_{wf} (2000 μS/cm) and σ_{ws} (50,000 μS/cm) are the assumed electrical conductivities of freshwater and seawater, and Archie's law at saturation was used, with pure sodium chloride being the only considered salt species and with the formation factor F = 4.8 [see, e.g., *Lebbe*, 1999; *Nguyen et al*., 2009; *Henderson et al*., 2010; *Herckenrath et al*., 2012], proportionality constant a = 1 and sedimentation exponent m between 1.1 and 1.3 for unconsolidated sediments [*Schön*, 2004]. Here Archie's empirical parameters are representative of high hydraulic conductivity values for unconsolidated sediments.

A temperature dependence formulation of σ_w is theoretically required if large temperature gradients are considered [e.g., *Hayley*, 2010]; however, here in this case, the effect of temperature with depth has been neglected.

Once the bulk electrical conductivities were determined from the saline water distribution, we proceeded with forward modeling of the electrical resistances of the considered ERT survey. ERT modeling and imaging was performed using the finite element code CRTOMO developed by *Kemna* [2000].

The chosen electrode layout consisted of a 4400 m long surface line equipped with electrodes every 25 m. Different configurations exhibit different sensitivity patterns and signal-to-noise ratios [e.g., *Dahlin and Zhou*, 2004]. Dipole-dipole (DD) possesses a higher resolution but a weaker signal-to-noise ratio compared to other configurations, e.g., Wenner array, and was successfully used in the framework of SWI [e.g., *Ogilvy et al*., 2009; *Nguyen et al*., 2009; *Hermans et al*., 2012]. The tested measurement protocols in this study were a DD scheme comprising 3525 measurements, a similar scheme where one electrode out of the two were skipped (refers to as DD1/2), a Wenner Schlumberger scheme (refers to as WS) and a Gradient array one (refers to as GD). For the homogeneous case, uncorrelated Gaussian random noise with a standard deviation equal to 5% of the mean value of the modeled resistance values was added to the data to account for uncertainty in measurements and discretization. This is a typical error level found in field studies [e.g., *Ogilvy et al*., 2009] and is expected to be representative of an average noise level observed in coastal environments.

2.2. Heterogeneous Case

The second synthetic case study presents a layered coastal aquifer with an intrinsic permeability field characterized by a two-facies system. The first features a high-permeability facies (log_{10} (k) (m^2)) that varies smoothly from −10 to −7.8. The style of heterogeneity is seemingly random heterogeneous porous media such as that found in, for example, *Hughes et al*. [2010]. A value of −13 for log_{10} (k) is prescribed for the second facies. In the latter, the variability of k is not of interest because of its low sensitivity in the groundwater model and the inability of ERT to detect such formations in a highly conductive medium. Given the permeability values, we computed a reference hydraulic conductivity field taking the density of freshwater into account. In HGS, the constitutive equations in variable-density flow are expressed in terms of freshwater properties (i.e., equivalent freshwater heads). For this reason, we also considered the freshwater hydraulic conductivity. It is also assumed, for the purposes of this study, that the viscosity of saltwater is the same as that of freshwater.

The model was refined in the vertical direction to 1.35 m in order to better account for heterogeneity, but kept unchanged in the *x* direction to save time when rendering out a big mesh. Boundary conditions were similar to the homogeneous case study. The pumping well was screened in the upper 12 m and placed at 1200 m from the ocean, with an average value of 14.5 m^3/d/m and a uniformly distributed recharge of 0.3 m/yr/m on the top of the aquifer. The model parameters used in the benchmark simulation were heterogeneous horizontal and vertical hydraulic conductivities, $K_h = 9.09 \times 10^{-3}$ m/s and $K_v = 9.09 \times 10^{-4}$ m/s for facies 2, $K_h = 9.18 \times 10^{-7}$ m/s and $K_v = 9.18 \times 10^{-9}$ m/s, for facies 1, and longitudinal and transversal dispersivities $\alpha_L = 4.57$ m and $\alpha_T = 0.91$ m, for facies 2, $\alpha_L = 45.71$ m and $\alpha_T = 9.14$ m, for facies 1, respectively. The simulation ran for 50 years in transient conditions from time zero up to reaching steady state. As the simulation ended, no changes were observed in concentration or hydraulic head, or in the intruding part of the seawater wedge. A simulation time of 50 years was necessary to produce an upconing (Figure 3a).

An empirical relationship [*Koukadaki et al*., 2007] was used to relate the simulated permeability, *k* (m^2), to bulk electrical conductivity, σ_b. *Huntley* [1986] emphasizes that this kind of relationship should be used with some caution because of its restricted applicability under the following circumstances: (1) when the geologic environment slightly changes and if the fluid salinity is not constant; (2) if any clays are present; or (3) if the apparent formation factor varies with fluid salinity. In this study, we have assumed a near-constant fluid salinity, a clay-free porous media and an effective formation factor which is independent of pore

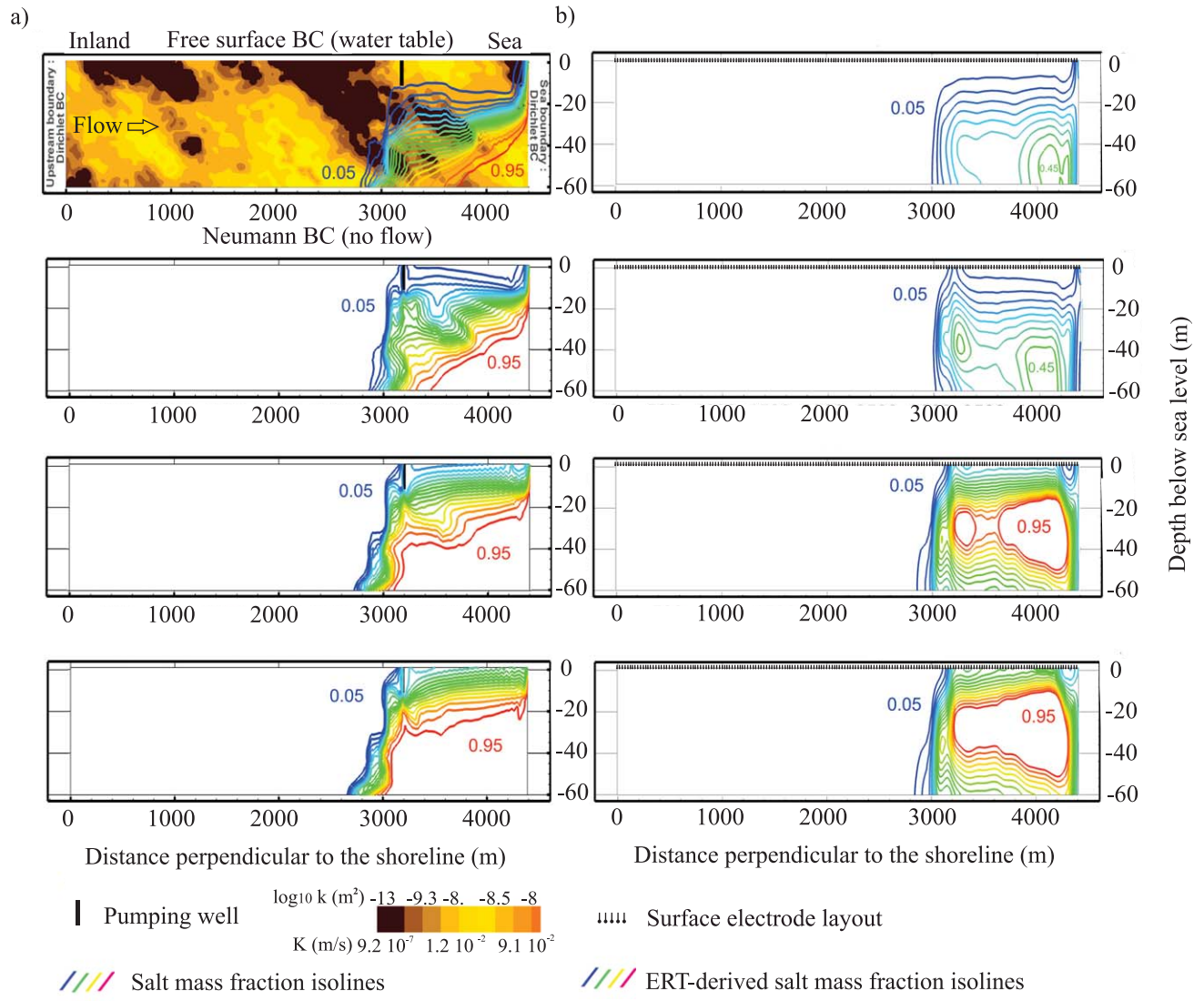

Figure 3. (a) Domain geometry with boundary conditions for the true heterogeneous SWI model and results of the simulation at steady state, after 1, 10, and 50 years (from top to bottom). (b) ERT-derived SMF model for the corresponding times.

water-related electrical conductivity and surface electrical conduction on water conductivity. According to several authors [e.g., *Archie*, 1942; *Schlumberger*, 1989], the permeability, k, and the porosity Φ may be related through an empirical relationship given by equation (1):

$$k = a_2 \Phi^{b_2} \tag{1}$$

where a_2 and b_2 (dimensionless) are experimental coefficients that depend on the rock type. We set a_2 to 1 and b_2 is set to 20 as suggested by *Barnabé et al.* [2003] for sandstone facies.

Using equation (1) together with Archie's law, we obtain a relationship that relates bulk electrical conductivity to permeability:

$$\sigma_b = \left(\frac{k}{a_2}\right)^{\frac{m}{b_2}} \frac{\sigma_w}{a} \tag{2}$$

Here surface conductivity was not specifically considered when converting permeability into bulk electrical conductivity but it should be taken into account when the role of sediment surface electrical conductivity is not negligible.

Once the bulk electrical conductivities had been determined from the saline water distribution, we proceeded with forward modeling of the electrical resistances. The tested measurement protocols in this study were a DD scheme comprising 2977 measurements, a similar scheme where one electrode out two were skipped (DD1/2), a WS scheme and a GD array one. An uncorrelated Gaussian random noise (as described for the homogeneous case) was used.

3. Uncoupled Hydrogeophysical Inversion

3.1. Geophysical Imaging and Appraisal

The geophysical inversion process (Figure 1) was based on a smoothness-constrained inversion algorithm [e.g., *LaBrecque et al*., 1996] in which the objective function contains a measure of error-weighted data misfit and a measure of first-order model roughness, balanced by a regularization parameter. The inversion problem was solved using an iterative Gauss-Newton scheme. The iteration process was stopped when the final root-mean-square (RMS) value of error-weighted data misfit was equal to 1 for a maximum value of the regularization parameter.

To calculate the ERT-derived SMF (Figure 1), we assumed the petrophysical relation to be known and used the Archie's law only. Different formation factors could be used if ERT is supposed to image different hydrogeologic structures (e.g., clay lenses). The results of this conversion are illustrated in Figures 2b and 3b for the considered homogeneous and heterogeneous aquifer cases, respectively.

In geophysical inversion, images suffer from variable resolution. In order to include this variation of resolution in the hydrogeophysical uncoupled inversion, we chose to use cumulative sensitivity as an indicator of ERT-derived SMF reliability. *Cassiani et al*. [1998] demonstrated that sensitivity could be used as an image appraisal tool to delineate well-recovered areas. More recently, *Caterina et al*. [2013] and *Hermans et al*. [2012] suggested that the cumulative sensitivity matrix can be used instead of the parameter resolution matrix. As an illustrative example, *Nguyen et al*. [2009] showed that electrical imaging can be used to characterize SWI if image appraisal tools, such as the cumulative sensitivity matrix, are appropriately used to account for the spatial variation of sensitivity, and thus resolution. This alternative is computationally inexpensive and provides a valuable insight into the resolution issue. It is based on the data error-weighted cumulative sensitivity vector, where the spatially distributed sensitivity of all individual measurements is lumped into absolute (squared) terms, **S**, according to *Kemna* [2000]. Hereafter this measure will be referred to simply as "the sensitivity":

$$\mathbf{S}=\sum_{i=1}^{n}\left[\frac{(J)_{ij}}{\epsilon_i}\right]^2=diag(\mathbf{J}^T\mathbf{W}_d^T\mathbf{W}_d\mathbf{J}) \tag{3}$$

with

$$J_{ij}=\frac{\partial d_i}{\partial m_j} \tag{4}$$

where **S** is based on the derivative with respect to the block resistivity (resistivity parameter $m_j=log(\rho_i)$) and ϵ_i is the individual (uncorrelated) data error.

Following the approach of *Nguyen et al*. [2009], a threshold value may be identified below which parameters are not sufficiently resolved. This threshold value refers to the sensitivity in equation (4) normalized to the maximum occurring value to range sensitivity from 0 to 1. More recently, *Caterina et al*. [2013] highlighted the possible difficulty in defining such a threshold when the discrepancy between the true and inverted models (e.g., SMF and ERT-derived SMF) does not show a significantly sharp increase along with the appraisal indicator. In this case, the threshold was determined on the mean normalized absolute error curve as being the most significant breakdown limit characterized by a general sharply growth trend in Figures 4a and 4c. We observed that the mean normalized absolute error on the recovered SMF increased more rapidly from the chosen threshold value. This threshold is chosen to validate the sensitivity-filtered ERT-derived SMF with enough reliability (low desired level of confidence) and to prevent, as far as possible, the selection of ERT-derived SMF with too large an individual normalized absolute error (i.e., poorly resolved parameters). We used a constant threshold value of $10^{-2.5}$ and 10^{-3} for the homogeneous and the heterogeneous case study, although a common value of $10^{-2.5}$ would have

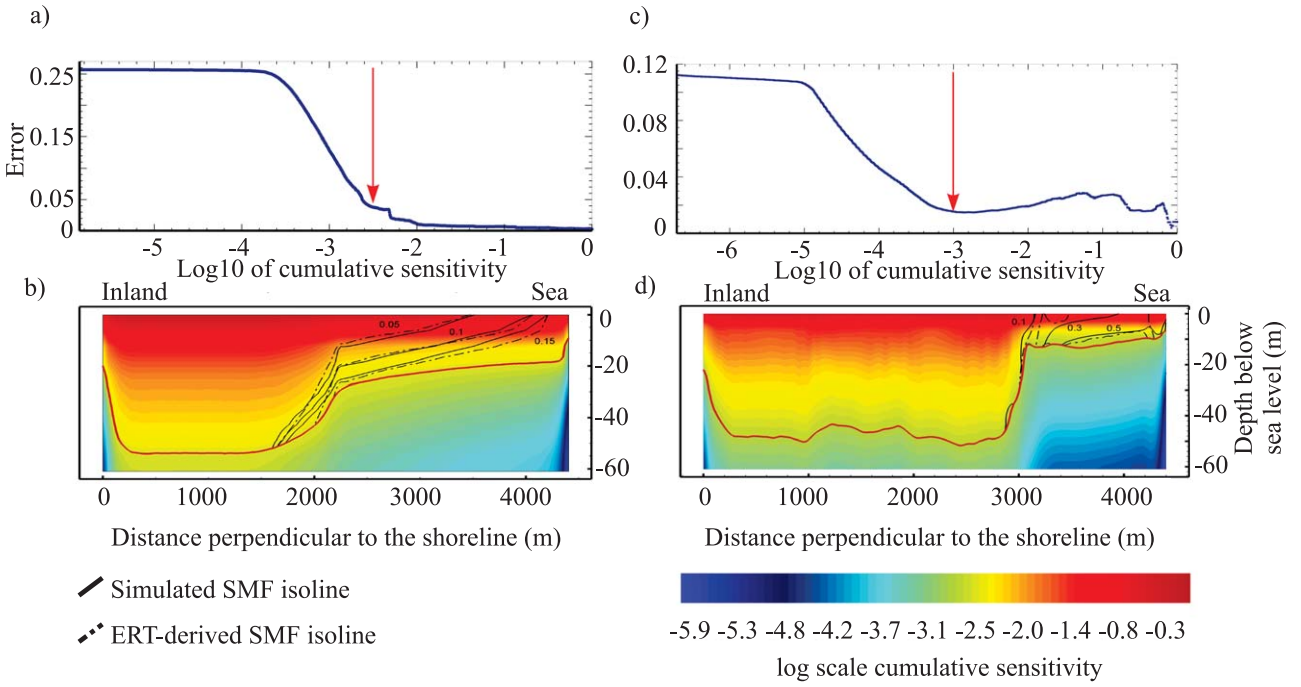

Figure 4. Mean normalized absolute errors on recovered SMF against the cumulative sensitivity distribution for the (a and b) homogeneous and (c and d) heterogeneous case study. The highlighted contour line corresponds with the chosen threshold (red arrow) of $10^{-2.5}$ and 10^{-3}.

been acceptable as well (Figure 4). Indeed, the region of acceptable parameter recovery does not notably change as we move from $10^{-2.5}$ to 10^{-3}. Beyond these chosen thresholds, recovered SMF values are deviating from the true SMF values. In the homogeneous case, the chosen electrode configuration allowed the recovery of mass fractions up to about 0.2 correctly, and up to 0.45 for the heterogeneous case (where the seawater interface is more affected by the pumping well). The relative number of satisfying recovered parameters is somewhat less than that observed by *Nguyen et al.* [2009], who used additional borehole electrical data while here this study focuses on surface data only. Indeed, the use of ERT data in boreholes (e.g., cross-hole measurements) provides higher resolution and increase sensitivity with depth [see, e.g., *Henderson et al.*, 2010]. The differences in the recovery emphasize that the selection of ERT-derived data is not trivial since sensitivity depends on both case-specific conditions (given resistivity distribution) and the chosen electrode configuration. For real data, calibrating an appraisal sensitivity indicator is discussed in section 5.2 in further details.

3.2. Hydrogeological Parameter Estimation

Calibration of the SWI model was undertaken targeting longitudinal dispersivity and horizontal hydraulic conductivity. It was performed by using the ERT-derived saline distribution within the software PEST [*Doherty*, 2004], which numerically computes the Jacobian of HGS by finite differences. The inversion algorithm is a standard gradient-based solver, which minimizes the following objective function using a Levenberg-Marquardt approach:

$$\phi=(\mathbf{c}-\mathbf{c}_i-\mathbf{J}(\mathbf{b}-\mathbf{b}_i))^T\mathbf{Q}(\mathbf{c}-\mathbf{c}_i-\mathbf{J}(\mathbf{b}-\mathbf{b}_i)) \quad (5)$$

where $\mathbf{c}$ is the data vector (conventional SMF data from wells and ERT-derived SMF), $\mathbf{c}_i$ is the model-calculated observations, $\mathbf{b}$ the parameter vector (hydraulic conductivity and dispersivity) with ($\mathbf{b}$-$\mathbf{b}_i$) the parameter upgrade vector, $\mathbf{Q}$ a diagonal weighting matrix associated with the data uncertainty, and $\mathbf{J}$ the Jacobian matrix. The index i refers to the ith model iteration.

In equation (5), each weight should be inversely proportional to the standard deviation of the associated observation [*Doherty*, 2004]. In order to compute a standard deviation that can be used to calculate the

Table 1. Fixed and Free Hydraulic Parameters for Cases 1 and 2[a]

	Value
Fixed Parameters	
ϕ	0.35
K_h/K_v	10
α_L/α_T	5
Q_{SMF}	392
$Q_{ERT-derived\ SMF}$	65
Free/Initial Parameters	
K_h (m/s)	6×10^{-3}
K_{h1} (m/s)	8×10^{-7}
K_{h2} (m/s)	3×10^{-3}
α_L (m)	50
α_{L1} (m)	5
α_{L2} (m)	50

[a]ϕ: effective porosity; K_h, K_v: horizontal and vertical hydraulic conductivity; α_L, α_T: longitudinal and transversal dispersivity; Q: data weights.

weights, we used a simple statistical framework [see, e.g., *Hill and Tiedeman*, 2007, chapter 11]. We assumed that the SMF well data are accurate within 0.5%, and ERT-derived SMF are accurate within 3%, corresponding to an average error level given the chosen threshold (Figure 4). The errors were assumed to be independent and normally distributed. Based on a 95% confidence interval (CI), two standard deviations of 0.0026 and 0.0153 were calculated corresponding for the entries of **Q** (weights) to 392 and 65, respectively. Although this way of calculating weights is approximate, regression results are not highly sensitive to moderate changes in the weighting [*Hill and Tiedeman*, 2007].

In this study, transversal dispersivity and vertical hydraulic conductivity do not play a part in the parameter estimation process. We fixed the ratio of dispersion anisotropy to 5 and horizontal-to-vertical hydraulic conductivity anisotropy to 10 (100 for facies 1). The initial estimates for the PEST objective function are given in Table 1.

3.3. Conceptual Models and Temporal Sampling

A number of different conceptual models can be defined, simplifying the domain with a minimum number of homogeneous representative hydrological units characterized by parameters, which are sensitive to the dynamic of the hydrogeophysical process. For the homogeneous case, a homogeneous hydrological model was used. For the heterogeneous case, four simplified hydrological models were built:

1. The low K facies is identified on the basis of the geophysical resistivity model as illustrated in Figure 5. It is data dependent and hence it may be different for another measurement protocol. More importantly, it helps to detect the presence and the lateral continuity of heterogeneities more accurately than borehole data generally do. Selection of a two-facies system was based on the expected resistivity values and contrast of buried structure depending on the ERT image resolution/sensitivity.

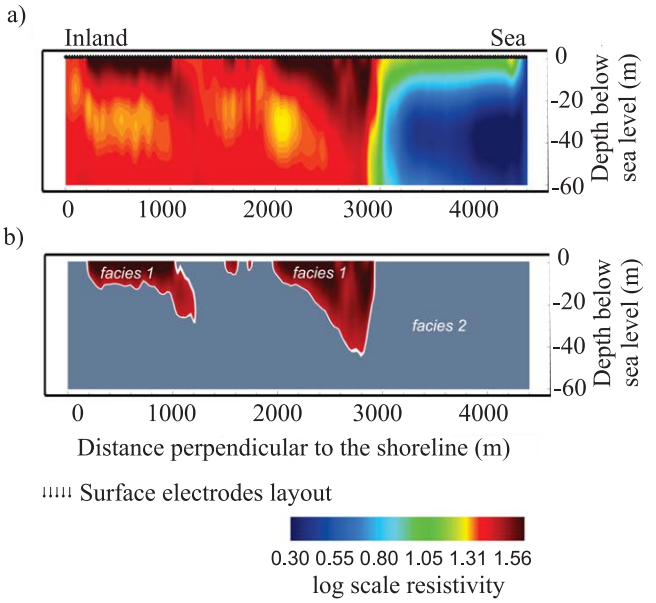

Figure 5. (a) Inverted resistivity model that corresponds with the SWI model after 50 years of pumping. (b) Conceptual model definition based on ERT.

2. The low K facies was identified on the basis of the synthetic borehole data and available a priori information (e.g., dipping structure) assuming that a well logging was carried out over the depth of the aquifer during drilling (Figure 8g). This facies matches the reference low K facies but arbitrarily thins and pinches as it extends reasonably far from the well.

3. The two models described above were combined to mimic a representative conceptual model (Figure 8j).

4. Finally, a reconstructable SWI benchmark model was based on the ERT-derived conceptual model (Figure 8l). This model is geophysically and hydrogeologically acceptable in that the reference and the ERT-derived low K facies are the same. Hereafter we will refer to it simply as the "no model error" scenario.

Indeed, parameterization based on geophysical data alone may inevitably produce model errors if complete information about the groundwater system is not available [*Hill and Tiedeman*, 2007]. Here geophysical data are used to support prior information and to build the most representative conceptual model possible.

The observations used for the calibration derive first from steady state and subsequently from time-lapse data (1 and 5 months, 1, 5, 10, 15, 20, 25, 50 years) and span over 50 years. *Herckenrath et al*. [2012] considered a semisynthetic case study and calibrated a SWI model stressed by a pumping well over 67 years, equivalent to the period between the establishment of a water supply well and the time in which TDEM (time domain electromagnetic method) data were collected. *Cheng and Ouazar* [2004] emphasize strongly that the development and testing of SWI hydrogeological models depend on long-term pumping records, as the response time of SWI interface is slow and might well be decades, or even a century or more. Some authors [e.g., *Werner and Simmons*, 2009] predict that the dynamics of the saline interface may be affected by sea level rise over the next hundred years. Other authors [e.g., *Morrow et al*., 2010] increasingly suggest that geophysical methods such ERT or cross-borehole resistivity tomography may be successfully used within the context of climate change. In the present study, selection of transient data was motivated by their representativeness in terms of seawater/freshwater interface dynamics. In practice, a pumping and upconing (pumping into the freshwater) or downconing (pumping into the seawater) tests in a coastal aquifer could be performed over a relatively short (but sufficiently long) time period [e.g., *Van Meir and Lebbe*, 2005] at a smaller scale. For practical applications, the installation and maintenance of long-term hydrogeophysical observatories will remain a challenge.

4. Calibration Results

Seeking an optimal method for data acquisition involves finding the best way to retrieve the correct estimation of the SMF as well as the transition zone geometry and hydrogeological parameters. This assessment should be based on different scenarios both in terms of spatial and temporal sampling. In the present case, we started by investigating the temporal sampling as this is the main concern when calibrating a transient SWI hydrogeological model. Following this, we tested different data acquisition procedures based on spatial sampling alone, using three different protocols as discussed in sections 2.1 and 2.2.

To test our first approach, we considered six different scenarios for calibrating the SWI models:

- In scenario 1, we considered salt concentration measurements at 10 different depths in the well.
- In scenario 2, we used ERT-derived SMF with no thresholding on the sensitivity (i.e., the entire ERT image) to calibrate the SWI models.
- In scenario 3, we used a threshold on the ERT-derived SMF, and calibration was performed on these sensitivity-filtered ERT images.
- In scenario 4, both sensitivity-filtered ERT images and salt concentration measurements in the well were included in the parameter estimation process.
- In scenario 5, we compared scenario 3 with the use of steady state data only. The latter was reached after 50 years of simulation in both cases.
- In scenario 6 (similarly to scenario 3), we used a threshold on a much noisier ERT-derived SMF data set, particularly for the homogeneous case. For the heterogeneous case, we used a conceptual model known a priori with the same noise level than in scenario 3.

For each scenario, all the data were of the same type, i.e., ERT-derived SMF or well-based SMF. Nevertheless, the data may be prone to different experimental errors. Indeed, the more certain measurements (salt concentration measurements, SMF) and those associated to a higher (but still acceptable) uncertainty (ERT-derived SMF) are associated with different weights in the parameter estimation process.

The results of the inverse calibration for the two benchmarks were assessed in terms of root mean square error (RMS):

$$RMS(\mathbf{b}) = \sqrt{\phi(\mathbf{b})/(ND+NPR-NP)} \tag{6}$$

where ϕ is the global data misfit defined in equation (5), ND is the number of ERT-derived SMF and/or well-based SMF used for inverse calibration (i.e., observations with nonzero weight), NPR is the number of prior

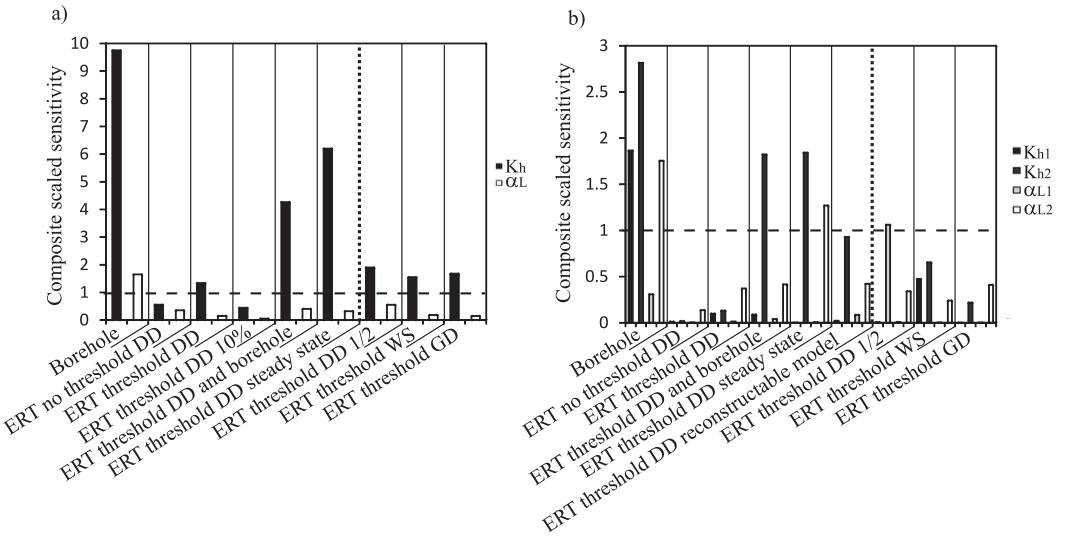

Figure 6. Composite scaled sensitivities for (a) the homogeneous case scenarios and (b) the heterogeneous case scenarios.

information values with nonzero weight, NP is the number of estimated (adjustable) parameters, and ***b*** is the parameter vector comprising hydraulic conductivity (K) and dispersivity (α) values.

In addition, the parameter correlation coefficient (pcc) and a composite scaled sensitivity (css) are used to investigate the uniqueness of the results:

$$pcc_{ij} = (Cov(\mathbf{b}_{ij})/(Var(\mathbf{b}_{ii})^{1/2} * Var(\mathbf{b}_{jj})^{1/2}) \tag{7}$$

where pcc_{ij} coefficients are calculated as the covariance between two parameters divided by the product of their standard deviations, and:

$$css_j = (\mathbf{Q}(\mathbf{J}\mathbf{J}^T))_{jj}^{1/2}/ND \tag{8}$$

where css_j is the composite scaled sensitivity for the jth parameter calculated for ND observations, **Q** and **J** are defined in equation (5).

Finally, individual linear 95% CI along with reasonable ranges are calculated to evaluate uncertainty of the parameter estimates:

$$95\%CI = b_j \pm t(n, 1.0-\alpha/2) * s_{b_j} \tag{9}$$

where b_j is the unknown jth parameter, $t(n, 1.0 - \alpha/2)$ is the Student t-statistic for n degrees of freedom at a significant level of α; n is the degree of freedom, here equal to ND + NPR − NP, α is equal to 0.05; and s_{b_j} is the standard deviation of the jth parameter.

More accurate nonlinear intervals [e.g., *Vecchia and Cooley*, 1987] can be calculated for these numerical models but they would require substantial execution time [*Doherty*, 2004; *Hill and Tiedeman*, 2007]. Comparison between the 95% CI, the true value, and the reasonable range is useful in that it may obviate an unnecessary search for model errors. For the homogeneous model, the range for the hydraulic conductivity was chosen between 2.74×10^{-4} and 1.14×10^{-2} m/s. For the longitudinal dispersivity, the range was taken from 15.24 to 50 m [*Huyakorn et al.*, 1987]. For the heterogeneous model, the same ranges were chosen for facies 2. For facies 1, the range for the hydraulic conductivity was chosen between 1×10^{-8} and 1×10^{-6} m/s. For the longitudinal dispersivity, it was chosen 10 times smaller than used for facies 2.

4.1. Sensitivity Analysis

In scenario 1, sensitivity analysis showed that most of parameters are more likely to be closely estimated with a low 95% CI (Figure 6). For all other scenarios in the homogeneous case study, sensitivity analysis generally highlighted the largest values for parameters K_h and parameters α_L as often being insufficiently

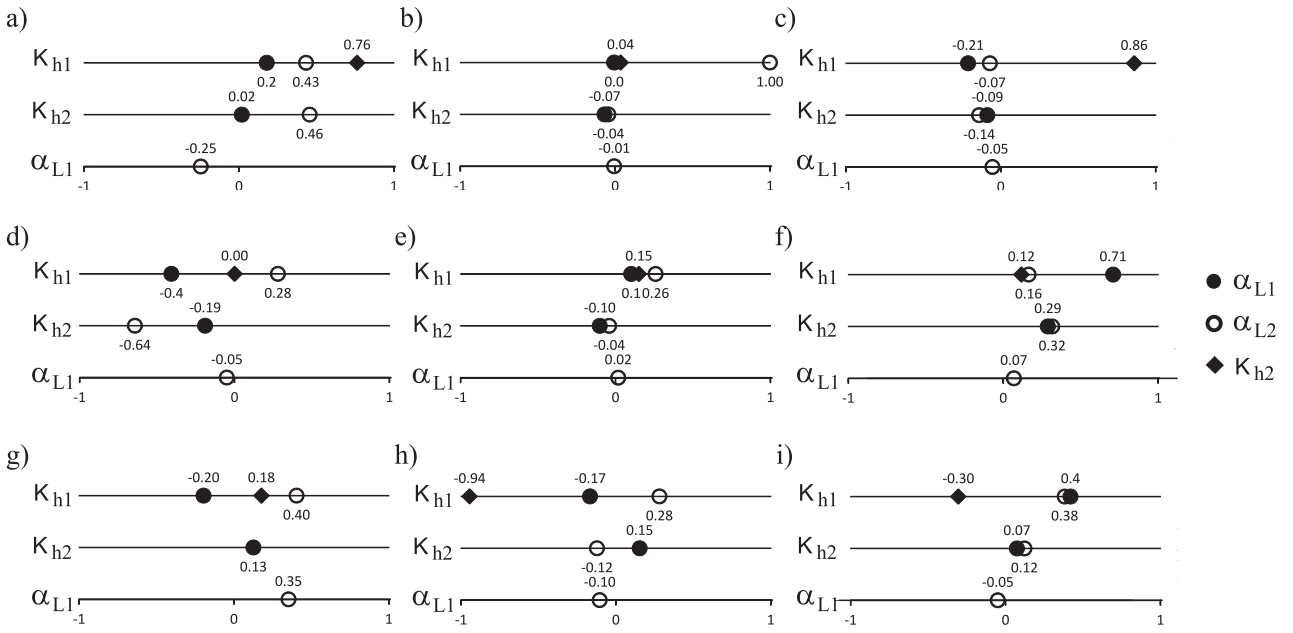

Figure 7. Parameter correlation coefficient for the heterogeneous scenarios. (a) Scenario 1: borehole data only, (b) scenario 2: all the ERT image—no threshold, (c) scenario 3: thresholding of the ERT surface only data (transient), (d) scenario 4: thresholding of the ERT surface only data and borehole data, (e) scenario 5: thresholding of the ERT surface only data (steady state), scenario 6: (f) thresholding of the ERT surface only data (transient, reconstructable conceptual model), (g) thresholding of the ERT surface only data (transient, DD1/2), (h) thresholding of the ERT surface only data (transient, WS), (i) thresholding of the ERT surface only data (transient, GD).

sensitive to the ERT-derived SMF (Figure 6a). In the heterogeneous case study, parameters of facies 2 are the most sensitive while parameters of facies 1 remain poorly sensitive (Figure 6b). Here css was used in a comparative manner within each scenario, but should not be used to draw comparisons between scenarios.

Figure 7 illustrates the calculated parameter correlation coefficients for the heterogeneous case study. Any combination between hydraulic conductivity and dispersivity for scenarios 1–6 and three extra scenarios (see section 4.4) are considered. This figure clearly shows that ERT-derived SMF could uniquely estimate all of the parameters, except for scenario 2. In scenario 3, the calculated high parameter correlation coefficient between K_{h1} and K_{h2} may make any conclusions difficult (Figure 7c) while it is not the case for scenario 5. For the latter, correlations remain very low. However, we note that the high parameter correlation coefficient in scenario 3 is lower than the critical value 0.95. All other scenarios show relatively low parameter correlation coefficients.

4.2. Calibration Results for the Homogeneous Case

In scenario 1 (borehole only, see Table 2), PEST recovered K_h and α_L accurately. Both interfaces coincide perfectly, indicating that borehole data alone would be sufficient to control the problem (Figure 8a).

Without thresholding the ERT-derived data (scenario 2), the recovered hydrogeological values within the 95% CI did not match the true values for either the hydraulic conductivity or the dispersivity (Table 2). The interface differs significantly from the true one (Figure 8b). In particular, neither the interface toe nor the transition zone, nor even the upconing, were well retrieved.

In scenario 3, we used a threshold on the sensitivity. The PEST inversion recovered K_h accurately and underestimated α_L (Table 2). In accordance with the α_L and α_T estimation, the estimated transition zone was found to be vertically slightly sharper than the simulated interface (Figure 8c). However, some SMF isolines were close to the simulated ones at the interface toe and seepage face.

In scenario 4, we used both surface sensitivity-filtered ERT and borehole data (Figure 8d). The correlation observed between the sensitivity above a certain threshold and the residuals between the ERT-derived and true SMF values allowed us to appropriately combine the two data sets. For the transient state, the results of the inversion are reasonably close to the true values with lower uncertainty on the parameters (Table 2). As expected, the interface closely matched the true values, as for the first scenario.

Table 2. PEST Results for the Homogeneous Case Study[a]

	True	Estimated	95% CI
Borehole Data			
Transient (RMS:0.3)			
K_h (m/s) ($\times 10^{-3}$)	7.06	7.06	7.05–7.07
α_L (m)	45.71	46.10	45.70–46.49
ERT Data			
Transient (RMS:23.8)			
K_h (m/s) ($\times 10^{-3}$)	7.06	3.34	2.78–4.02
α_L (m)	45.71	281.30	210.54–375.83
Transient (threshold) (RMS:3.2)			
K_h (m/s) ($\times 10^{-3}$)	7.06	9.77	8.91–10.71
α_L (m)	45.71	10.58	4.68–23.89
ERT and Borehole Data			
Transient (RMS:10.9)			
K_h (m/s) ($\times 10^{-3}$)	7.06	7.09	6.98–7.20
α_L (m)	45.71	17.91	9.91–32.34
ERT Data			
Steady state (threshold; RMS:1.8)			
K_h (m/s) ($\times 10^{-3}$)	7.06	8.87	8.00–9.83
α_L (m)	45.71	12.13	1.64–89.28
Transient 10% (threshold) (RMS:3.2)			
K_h (m/s) ($\times 10^{-3}$)	7.06	9.22	7.96–10.68
α_L (m)	45.71	8.26	2.51–27.16

[a] K_h: horizontal hydraulic conductivity; α_L: longitudinal dispersivity; *CI*: confidence interval; *RMS*: Root Mean Square Error.

In scenario 5, we compared scenario 3 with the use of a threshold on the sensitivity for steady state conditions. For the latter, the PEST inversion recovered K_h accurately, and underestimated α_L (Table 2). Even if static ERT-derived SMF are considered, the interface was almost entirely retrieved, both in terms of interface toe and transition zone (Figure 8e).

Finally, in scenario 6 (similar to scenario 3), we assumed a noisier resistance data set with an average noise level of 10%, i.e., uncorrelated Gaussian random noise with a standard deviation equal of 0.9Ω or 17% of the mean value of the modeled resistance values. The PEST inversion recovered K_h close to the true value and underestimated α_L (Table 2). Both estimations fall into a correct range around the true values in comparison to scenario 3, and the impact on the calculated interface is not visible (Figure 8f).

Figure 9 illustrates the comparison of parameter estimates and 95% CI with the reasonable range of parameter values, in order of appearance, for scenarios 3, 5, 6, and an extra scenario (see section 4.4 for the latter). The numerical values of the 95% CI can be found in Table 2. These scenarios emphasize the ability of ERT surface data alone to retrieve parameter values. In these scenarios (Figures 9a–9c), most of the ERT-derived SMF were underestimated, making the calculated interface sharper than expected. In Figures 9e–9g, the K_h parameter estimate and entire 95% CI lay within the reasonable range of values. In Figures 9e and 9g, the α_L parameter estimate was close to its reasonable range but the 95% CI partly lay in the reasonable values. In Figure 9f, half of the 95% CI lies within the reasonable range for the dispersivity parameter.

4.3. Calibration Results for the Heterogeneous Case

For scenario 1 (Table 3), PEST recovered K_{h1} for facies 1 at 1×10^{-5} m/s (parameter upper bound) but K_{h2} for facies 2 was estimated accurately. The corresponding dispersivity values α_{L1} and α_{L2} were both underestimated within the 95% CI. However, both interfaces closely match each other as a whole with the exception of the interface toe where the transition zone is sharper (Figure 8g).

In scenario 2, we used no threshold on the sensitivity. The recovered hydrogeological values within the 95% CI did not match the true values for either the hydraulic conductivity or the dispersivity (Table 3). In Figure 8h, the estimated interface moves away from the simulated one and shows artifacts on both sides of the interface.

In scenario 3, PEST recovered K_{h1} within 2 orders of magnitude, but poorly recovered K_{h2} at 1×10^{-7} m/s (parameter lower bound) with failed 95% CI (Table 3). The latter parameter was strongly underestimated, possibly due to the absence of the embedded facies 1 within the seawater wedge (Figure 8i). The corresponding dispersivity value α_{L1} and α_{L2} were both overestimated. Figure 8i illustrates that the interface seems to be retrieved both in terms of transition zone and interface toe.

In scenario 4, we used borehole data in addition to surface ERT data for the transient condition. The embedded facies 1 within the seawater wedge is still not taken into account except the two lowest lenses that intercept the well (Figure 8j). The PEST inversion recovered K_{h1} at 1×10^{-5} m/s (parameter upper bound) and K_{h2} within the correct order of magnitude. The corresponding dispersivity value α_{L1} was limited at 400 m (parameter upper bound) while α_{L2} was estimated accurately (Table 3).

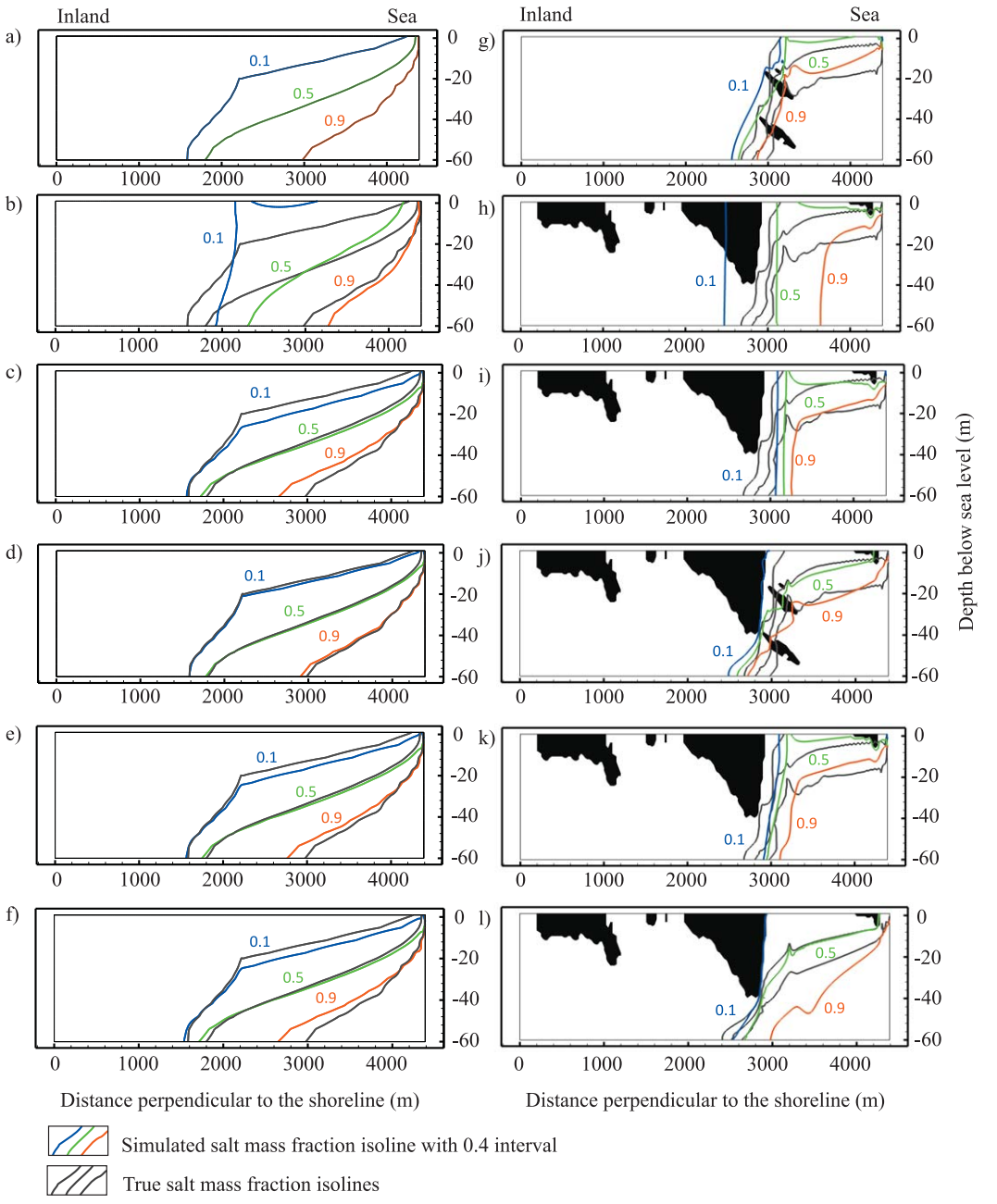

Figure 8. Calibrated results: The gray lines represent the true isolines. The colored lines represent the results of the calibration. (left) Homogeneous case. (right) Heterogeneous case. From top to bottom: (a and g) scenario 1, borehole data only; (b and h) scenario 2, all the ERT image—no threshold; (c and i) scenario 3, thresholding of the ERT surface only data (transient); (d and j) scenario 4, thresholding of the ERT surface only data and borehole data; (e and k) scenario 5, thresholding of the ERT surface only data (steady state); scenario 6, (f) thresholding of the ERT surface only data (transient, 10% of noise) and (l) thresholding of the ERT surface only data (transient, reconstructable conceptual model).

In scenario 5, we compared the use of a threshold on the sensitivity both for steady state and transient conditions. For the former, PEST underestimated K_{h1} with large 95% CI and the dispersivity value α_{L1} was estimated at 0.5 m (parameter upper bound; Figure 8k). Parameters for facies 2 were much better retrieved with steady state data alone than with transient data (Table 3). PEST failed to properly estimate the parameters for facies 1 in scenario 3, although the transient data were expected to improve the inverse calibration results significantly.

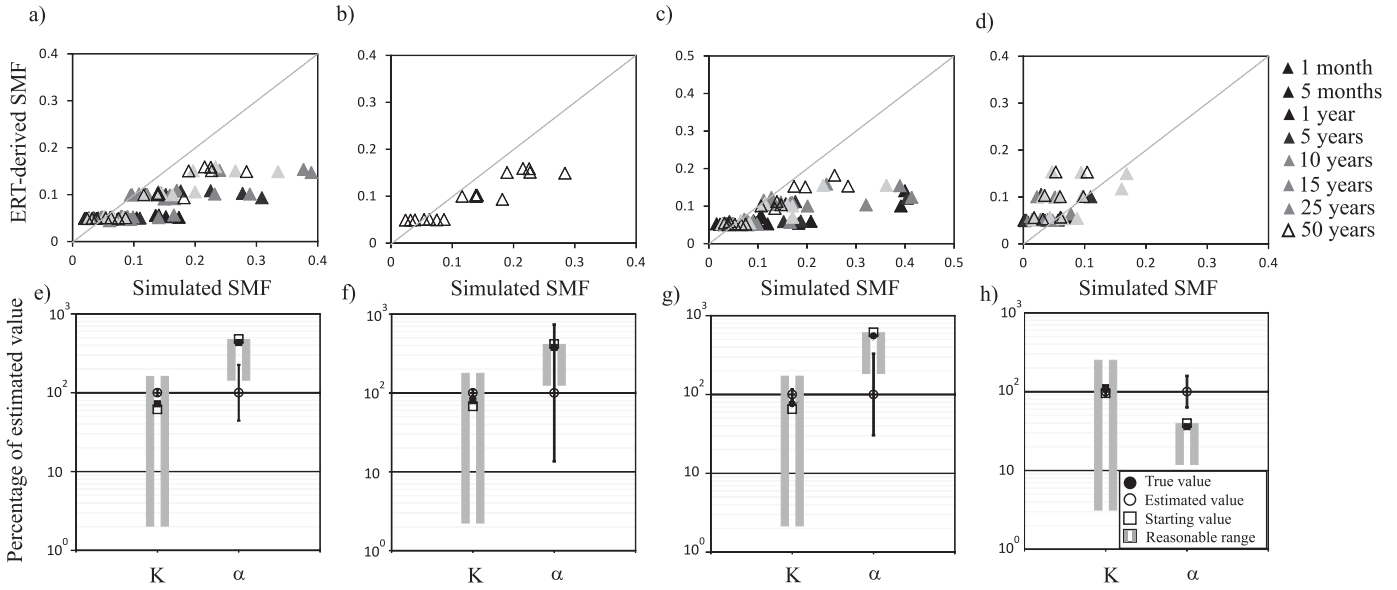

Figure 9. (top) ERT-derived SMF in function of the simulated SMF (calibration observations). (bottom) Starting (empty square), estimate (empty circle), true parameter values (black circle), linear individual 95% confidence interval (black bars), and limits of the parameters reasonable range (gray boxes), expressed as percentage of the estimated values. (a and e) Scenario 3: thresholding of the ERT surface only data (transient), (b and f) scenario 5: thresholding of the ERT surface only data (steady state), (c and g) scenario 6: thresholding of the ERT surface only data (transient, 10% of noise), (d and h) scenario DD1/2: thresholding of the ERT surface only data (transient, DD1/2).

Table 3. PEST Results for the Heterogeneous Case Study[a]

	True	Estimated	95% CI
Borehole Data			
Transient (RMS:30.6)			
K_{h1} (m/s) ($\times 10^{-7}$)	9.18	100	78.6–127.2
K_{h2} (m/s) ($\times 10^{-3}$)	9.09	1.23	1.06–1.44
α_{L1} (m)	4.571	2.53	0.96–6.69
α_{L2} (m)	45.71	33.66	27.90–40.61
ERT Data			
Transient (RMS:27.56)			
K_{h1} (m/s) ($\times 10^{-7}$)	9.18	100	12.7–782.3
K_{h2} (m/s) ($\times 10^{-3}$)	9.09	0.10	0.03–0.35
α_{L1} (m)	4.571	400	Failed
α_{L2} (m)	45.71	400	352–454
Transient (threshold) (RMS:12.03)			
K_{h1} (m/s) ($\times 10^{-7}$)	9.18	0.25	0.12–0.52
K_{h2} (m/s) ($\times 10^{-3}$)	9.09	0.0001	Failed
α_{L1} (m)	4.571	29.82	1.9–468.9
α_{L2} (m)	45.71	67.54	61.47–74.20
ERT and Borehole Data			
Transient (RMS:30.88)			
K_{h1} (m/s) ($\times 10^{-7}$)	9.18	100	39.26–254.65
K_{h2} (m/s) ($\times 10^{-3}$)	9.09	9.27	8.78–9.79
α_{L1} (m)	4.571	400	53.69–2979.57
α_{L2} (m)	45.71	40.01	31.37–51.02
ERT Data			
Steady state (threshold) (RMS:11.74)			
K_{h1} (m/s) ($\times 10^{-7}$)	9.18	0.21	Failed
K_{h2} (m/s) ($\times 10^{-3}$)	9.09	0.49	0.41–0.58
α_{L1} (m)	4.571	0.5	Failed
α_{L2} (m)	45.71	59.64	46.55–76.40
Transient DD reconstructable (threshold) (RMS:4.09)			
K_{h1} (m/s) ($\times 10^{-7}$)	9.18	79.84	9.32–683.97
K_{h2} (m/s) ($\times 10^{-3}$)	9.09	8.32	8.01–8.65
α_{L1} (m)	4.571	43.67	24.90–76.58
α_{L2} (m)	45.71	175.70	161.80–190.78

[a] K_{h1}, K_{h2}: horizontal hydraulic conductivity for facies 1 and facies 2; α_{L1}, α_{L2}: longitudinal dispersivity for facies 1 and facies 2.

In scenario 6, the conceptual model was built identically to the SWI benchmark ("no model error"). All recovered parameters were found to be close to the true values, although parameters of facies 2 remained poor in terms of sensitivity (Table 3 and Figure 8l).

Figure 10 illustrates the comparison of parameter estimates and 95% CI with the reasonable range of parameter values for scenarios 3, 5, 6, and an extra scenario (see section 4.4 for the latter). The numerical values of the 95% CI can be found in Table 3. In scenarios 3 and 5 (Figures 10a and 10b), the simulated interface is sharper than expected but results in slightly overestimated dispersivity values. In scenario 3, the K_{h2} parameter estimate and entire 95% CI lie outside the reasonable interval, while 95% CI of α_{L1} partly lies in the range of reasonable values (Figure 10e). In scenario 5, a comparison with steady state conditions shows that the K_{h1} parameter estimate is consistent having 95% CI within the reasonable range of values (Figure 10f). In scenario 6, the simulated interface is wider than expected, resulting in overestimated dispersivity values (Figure 10c). Figure 10g shows a good

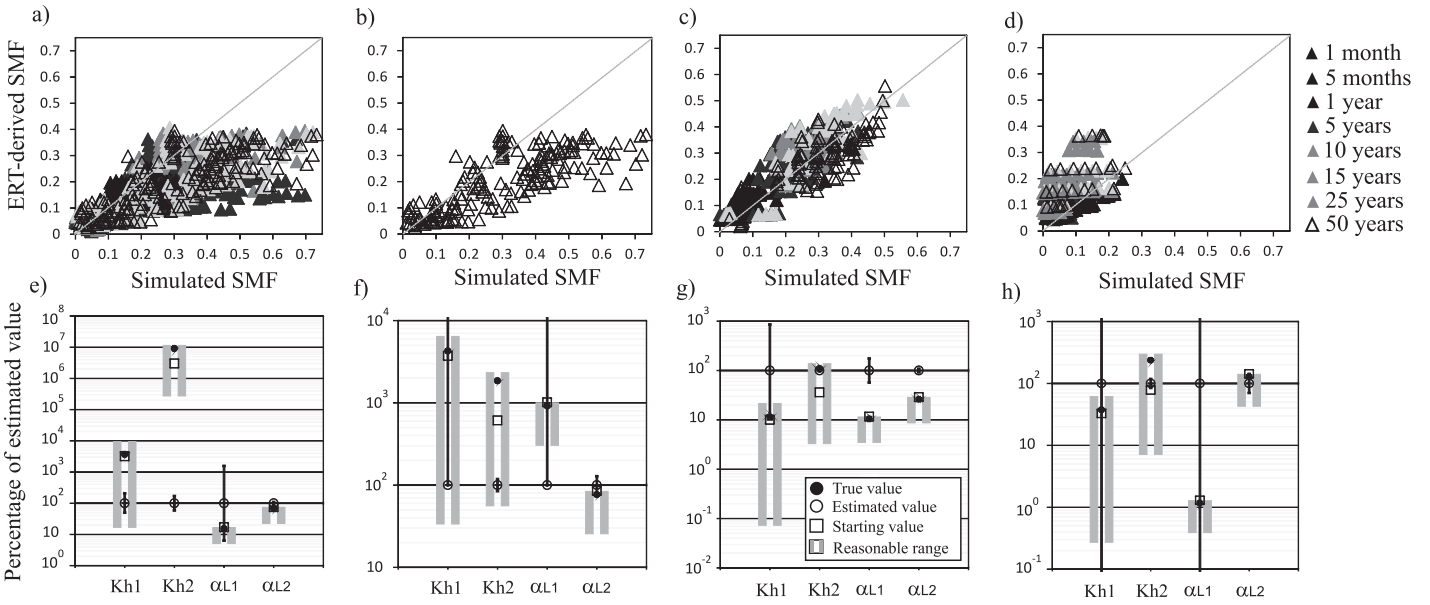

Figure 10. (top) ERT-derived SMF in function of the simulated SMF (calibration observations). (bottom) Starting (empty square), estimate (empty circle), true parameter values (black circle), linear individual 95% confidence interval (black bars) and limits of the parameters reasonable range (gray boxes), expressed as percentage of the estimated values. (a and e) Scenario 3: thresholding of the ERT surface only data (transient), (b and f) scenario 5: thresholding of the ERT surface only data (steady state), (c and g) scenario 6: thresholding of the ERT surface only data (transient, reconstructable conceptual model), (d and h) scenario DD1/2: thresholding of the ERT surface only data (transient, DD1/2).

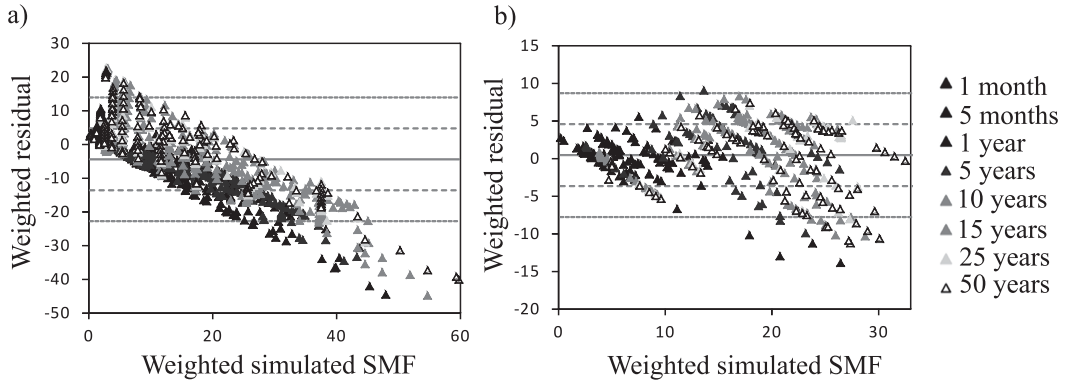

Figure 11. (a) Weighted residuals and weighted simulated values showing evidence of model bias for the third heterogeneous case scenario (model error, transient, DD) and (b) weighted residuals and weighted simulated values showing with no model bias for the sixth heterogeneous case scenario (no model error). The mean and the standard deviations of the weighted residuals are used to define grid lines for the weighted residuals.

correspondence between hydraulic conductivity parameter estimates in terms of range and 95% CI. However, the same is not the case for dispersivity.

Finally, the appropriateness of the representative conceptual model (scenario 6) in comparison to a nonreconstructable conceptual model (scenario 3) is illustrated in Figure 11 in terms of calibration results. Figure 11a shows a decrease trend between the weighted residual and the weighted simulated SMF, i.e., existence of a model bias. In Figure 11b, the model bias is nonexistent, in that the weighted residuals appear random with respect to the weighted simulated values.

4.4. Assessment of Geophysical Data Acquisition Strategies

We selected three different protocols commonly used in a SWI environment: first, a DD1/2; second, a WS protocol comprising 3235 measurements; and finally a GD protocol comprising 4236 measurements.

For the homogeneous case, we observe in Figure 12a that DD1/2 is generally able to retrieve much less ERT-derived SMF in comparison to the DD protocol. The WS and GD show the same general growth trend

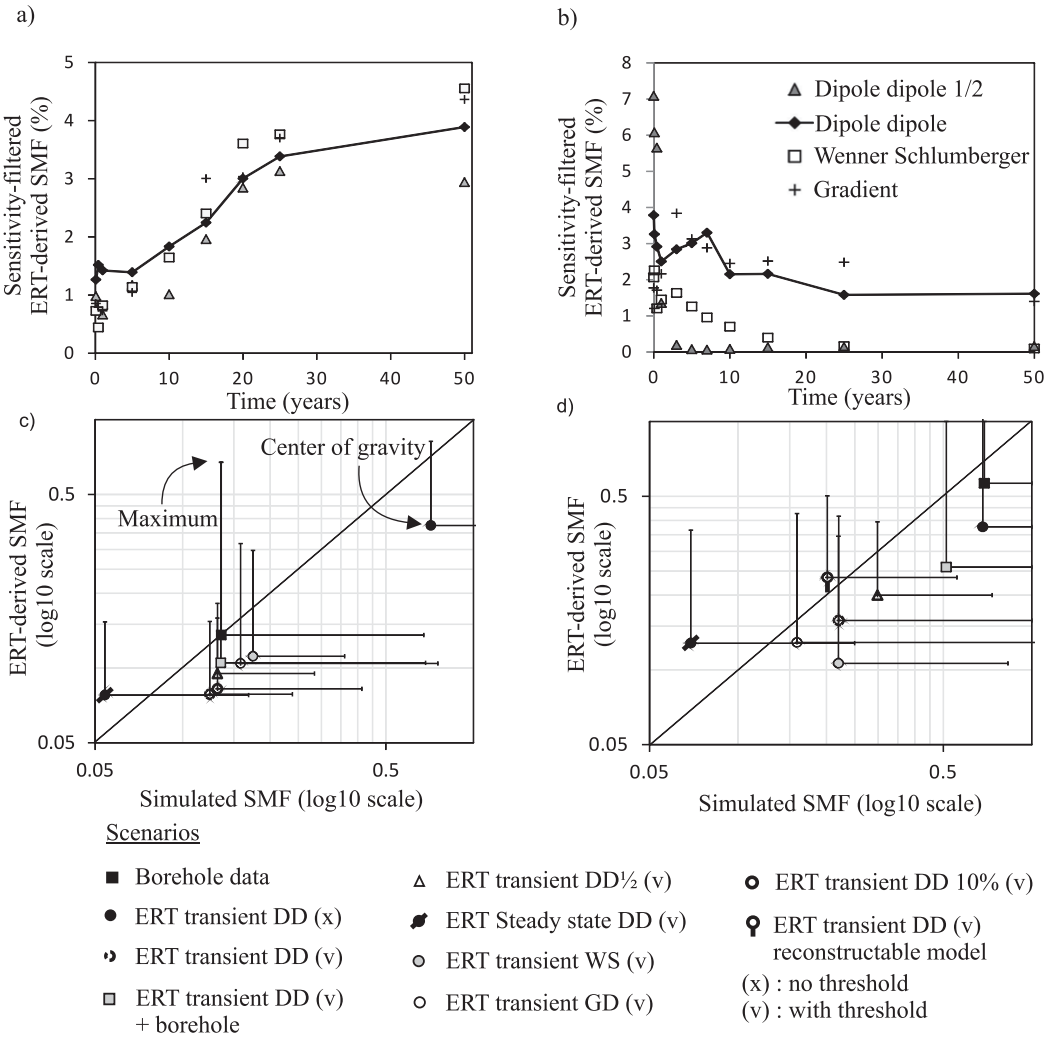

Figure 12. ERT data quality: percentage of sensitivity-filtered ERT-derived SMF for four different protocols (DD - DD1/2 - WS - GD) versus time (a) for the homogeneous case study, (b) for the heterogeneous case study, and scatter graph of sensitivity-filtered ERT-derived SMF versus simulated SMF (true values) (c) for the homogeneous case study and (d) for the heterogeneous case study. Cluster of points for each scenario is estimated with its center of mass. The maximum ERT-derived or simulated SMF is depicted by the upper half of a whisker.

as we move from time 0 up to 50 years. They allowed us to retrieve more ERT-derived SMF than the DD as the interface of SWI was getting close to the ground surface. For the heterogeneous case, we observe in Figure 12b that DD1/2 still shows the lower percentage of ERT-derived SMF with time except at the very beginning of the simulations. The WS and GD protocols exhibited more ERT-derived SMF than the DD1/2 but the GD protocol shows the same general decrease trend than the DD protocol. The general decreasing trend observed in the percentage of ERT-derived SMF is due to the extend of the transition zone. The latter became sharper in the heterogeneous case while it was wider in the homogeneous case.

The reliability of ERT-derived SMF in comparison to the simulated SMF is illustrated in Figures 12c and 12d for the homogeneous and heterogeneous cases, respectively. For the former, we observe that ERT-derived SMF (maximum values depicted as the upper half of a whisker) was somehow underestimated but the discrepancy for the DD, DD1/2, and WS remained low. However, the bias in the ERT-derived SMF for the DD1/2 protocol, expressed in term of center of mass, is more evident than the DD, WS, and GD protocols. For the heterogeneous case, although the center of mass of the GD is closer to the bisector, ERT-derived SMF was lower than expected. The DD1/2 still show the most consistent ERT-derived SMF.

In all scenarios, we used a threshold on the sensitivity. Results are illustrated in Figures 9d, 9h, 10d, 10h, for the DD1/2 protocol and Figure 13 for the DD1/2, WS,GD protocols and summarized in Tables 4.

Table 4. PEST Results for Geophysical Data Acquisition Strategies[a]

	True	Estimated	95% CI
Homogeneous			
ERT data			
Transient DD1/2 (threshold) (RMS:4.1)			
K_h (m/s) ($\times 10^{-3}$)	7.06	6.29	5.51–7.20
α_L (m)	45.71	127.6	80.64–201.88
Transient WS (threshold) (RMS:3.9)			
K_h (m/s) ($\times 10^{-3}$)	7.06	9.87	8.67–11.12
α_L (m)	45.71	5.00	1.70–14.70
Transient GD (threshold) (RMS:3.4)			
K_h (m/s) ($\times 10^{-3}$)	7.06	9.14	8.10–10.30
α_L (m)	45.71	6.11	1.54–24.13
Heterogeneous			
ERT data			
Transient DD1/2 (threshold) (RMS:5.58)			
K_{h1} (m/s) ($\times 10^{-7}$)	9.18	24.50	Failed
K_{h2} (m/s) ($\times 10^{-3}$)	9.09	3.84	3.26–4.53
α_{L1} (m)	4.571	391.9	Failed
α_{L2} (m)	45.71	36.62	24.97–50.81
Transient WS (threshold) (RMS:15.02)			
K_{h1} (m/s) ($\times 10^{-7}$)	9.18	100,000	Failed
K_{h2} (m/s) ($\times 10^{-3}$)	9.09	18.97	4.91–73.27
α_{L1} (m)	4.571	0.5	Failed
α_{L2} (m)	45.71	21.7	5.26–85.14
Transient GD (threshold) (RMS:9.47)			
K_{h1} (m/s) ($\times 10^{-7}$)	9.18	24.69	Failed
K_{h2} (m/s) ($\times 10^{-3}$)	9.09	100	49–200
α_{L1} (m)	4.571	12.86	Failed
α_{L2} (m)	45.71	56.80	39.05–82.61

[a] K_h: horizontal hydraulic conductivity; α_L: longitudinal dispersivity; K_{h1}, K_{h2}: horizontal hydraulic conductivity for facies 1 and facies 2; α_{L1}, α_{L2}: longitudinal dispersivity for facies 1 and facies 2; *CI*: confidence interval; *RMS*: Root Mean Square Error.

In the homogeneous case, the WS and GD scenarios show that the calculated interface is sharper than expected because α_L is strongly underestimated. Although the WS and GD protocols contain more measurements, the DD1/2 goes deeper into the aquifer.

In the heterogeneous case, the WS and GD scenarios show that the interface toe of the seawater intrusion wedge does not match the simulated interface toe. This can be explained by the discrepancy between the ERT-derived SMF and the simulated SMF along with the existence of a model error deeper the aquifer.

Figure 13 suggests that skipping one electrode out of two for DD1/2 protocol provides sufficient information content to estimate the hydraulic conductivity of facies 2. In the homogeneous case, the css of parameters K_h was found to be over 1, while dispersivity still remained poor in terms of sensitivity for the three scenarios. Moreover, Figures 9d and 9h also suggest the K_h parameter estimate is to be more reasonable, although dispersivity was overestimated here. Although the latter is significantly high, the interface perfectly matched the simulated one. In the heterogeneous case, DD1/2 protocol enhanced the most sensitive parameter estimates (Figures 10d and 10h) but still suggests the need for additional deeper information when a model error exists.

5. Discussion

5.1. General Comments

For the homogeneous case, comparison of parameter estimates and 95% CI with the reasonable range of parameter values suggests that the estimate was acceptable (as shown by the calculated interface). Dispersivity parameter estimates seem unreasonable and systematically underestimated because of a likely model bias. Indeed, the ERT-derived SMF are biased in that the difference between the ERT-derived SMF and the high simulated ones is negative. However, we note that the calculated interface matches the simulated interface quite closely. Discrepancy observed in α_L stems from both its low css and the error level in the ERT-derived SMF, but also—and more importantly—from the lack of ERT-derived data over the full thickness of the aquifer and across the transition zone. This model error could be solved by correcting the input data (i.e., eliminating model bias in the observations) while the reasonable range could be estimated more precisely with additional data. Indeed, additional data and a priori information would improve the results significantly. The use of additional borehole data (water samples) would further improve the estimated parameters and reduce uncertainty considerably. Among the measurement protocols, the DD scheme seems to be the best protocol configuration in terms of spatial and time sampling to recover the mass fraction. The best compromise possible should be found with regard to the electrode layout and measurement setting; it should then be tested on a representative synthetic case study prior to real-life application.

For the heterogeneous case, the ERT-derived SMF image indicates that the model is indeed heterogeneous, whereas this can hardly be inferred from single-well data on a large scale. The calibration results points out

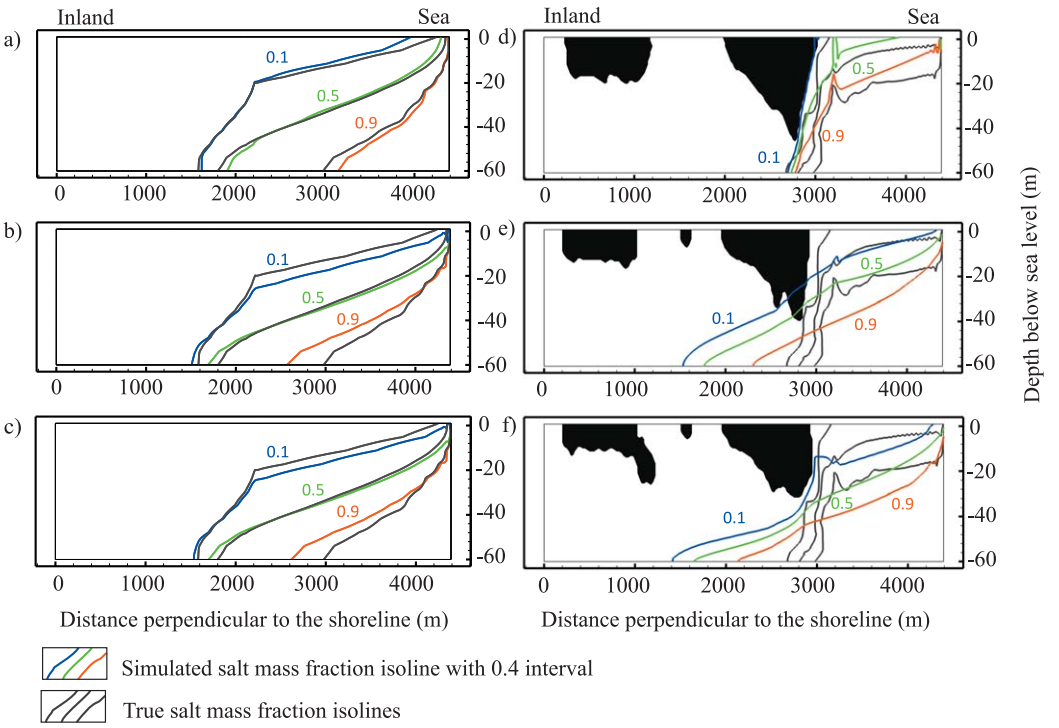

Figure 13. Calibrated results: the gray lines represent the true isolines. The colored lines represent the results of the calibration. (left) Homogeneous case. (right) Heterogeneous case. From top to bottom: (a and d) thresholding of the ERT surface only data (transient, DD1/2), (b and e) thresholding of the ERT surface only data (transient, WS), and (c and f) thresholding of the ERT surface only data (transient, GD).

poor estimation of parameters for facies 1 and relatively high RMS values. They show that either the data do not contain enough reliable information or that the conceptual model cannot reproduce the transport processes in terms of SMF isolines. Scenario 6, with a reconstructable conceptual model, shows a misfit lower than scenario 3. In the latter, final flow model misfit reveals significant modeling error, which cannot be accommodated by weighting or accounted for by the measurement error. DD1/2 scenario is good example. Thus, the unrealistic optimized value for facies 2 in scenario 3 cannot be attributed to the model error only, the evidence being that calibration results in both steady state (DD) and transient state (DD1/2) show realistic optimized values for second facies. This suggests that ERT-derived SMF are not sufficient to explain the existence of the model bias. Moreover, additional data would be needed to estimate the parameter of facies 1 more precisely. This also happens when using borehole data only at transient states. The conceptual hydrogeological model based on additional borehole data significantly improves the parameter estimates of the facies 2, while the parameters of facies 1 remain poorly recovered. In the total absence of model bias along with high-quality ERT-derived SMF, calibration results reveal realistic parameter estimate of facies 1 but still overestimates the dispersivity values. The latter might be overcome if the DD protocol was appropriately optimized, as is the case in the presence of a model error. Hydrogeologically speaking, the low sensitivity of these parameters and the significant uncertainty in the estimated values make proper calibration of this facies difficult if important model construction inaccuracies exist.

Comparison between static and dynamic approaches illustrates that both approaches allow the retrieval of transition zone and the interface toe. They estimate the parameters and their uncertainties within the same order of magnitude. ERT-derived transient data were not found to significantly improve the parameter estimation when using surface ERT data only.

5.2. Calibrating an Appraisal Sensitivity Indicator for Field Applications

We have demonstrated that it is possible to retrieve high-quality ERT-derived SMF if a threshold is appropriately set on the sensitivity indicator for a desired, but subjective, level of confidence (where the error on the model parameters is known). In the field, estimating the error of model parameters is one of the biggest

difficulties faced because the true resistivity distribution is generally unknown. An additional (and aforementioned) potential difficulty in selecting a threshold value is if the mean normalized absolute error curve does not show a general growth trend in the function of the sensitivity indicator. This threshold may be chosen arbitrarily based on the user experience. This threshold is to be determined experimentally using the breakdown limit observed in Figures 4a and 4c. Estimating the error model may be performed either on the basis of ground-truth information or with the creation of a synthetic model. Calibrating the sensitivity indicator involves using punctual 1-D information, e.g., sampled electromagnetic induction borehole logging data, in-hole ERT data or water samples [e.g., *Hermans et al*., 2012]. Water samples might also be appropriately gathered using some packer and subsequently used to calibrate the appraisal indicator. However, this option is expensive and requires a fully sampled well, which is quite rare and therefore uncommonly used in a real-life application. When no ground-truth data exist, an innovative in situ validation-dependent methodology derived from *Caterina et al*. [2013] can be used in order to quantitatively appraise an ERT image using the sensitivity indicator. In this methodology, numerical benchmarks models representing simplified cases of field ERT images can be built using available a priori information and used to define an approximate error model. This conceptual framework offers some clues about how to appraise an ERT image when an appraisal indicator cannot be set on the true error model.

6. Conclusions and Perspectives

This study has demonstrated that the reliability of estimated SWI model parameters with the uncoupled hydrogeophysical inversion approach depends on ERT image appraisal as well as hydrogeological model conceptualization. The results are only consistent if a well-defined threshold is applied on the cumulative sensitivity. We further demonstrated that the results are improved if salt concentration data from appropriately located multiscreen wells are used in addition to ERT-derived SMF. The acquisition of the latter can, however, be challenging in practice since we often do not have good a priori information about the position of the seawater wedge. Moreover, a fully sampled well is quite uncommon even when using packers, and can also lead to undesired fluxes into the well. This suggests that surface-ERT should be first choice to delineate heterogeneities and to identify appropriate positions of multiscreen wells. Subsequently, both wells and ERT-derived data should be used together for SWI model calibration in an inverse modeling framework.

The discrepancy observed in dispersivities stems from either the lack of ERT-derived data over the full thickness of the aquifer or its low sensitivity to ERT-derived SMF data. While, for the former, additional data and a priori information would improve the results significantly, ERT-derived SMF do not contain enough information to further constrain the estimation of dispersivity within low-sensitivity facies.

When calibrating a heterogeneous hydrogeological model, the most important source of error is the conceptualization of the hydrogeological model. This model bias was introduced by delineation of heterogeneities with geophysical data. Neglecting the embedded facies within the seawater wedge prevents from representing the transport processes that the model is able to produce and the inverse calibration cannot be properly performed (i.e., certain parameter estimates are unrealistic) with ERT-derived data alone. However, we have demonstrated, within the scope of an optimal data collection strategy, that the DD scheme is the most efficient measurement protocol if the electrode configuration is optimized. Moreover, calibration results suggest that the threshold should be calibrated along with time-lapse geophysical data acquisition to eliminate possible model bias in the ERT-derived SMF. Evidently, calibration processes can also be properly performed if no model error exists, because only the error level on the high-quality ERT-derived transient data contributes to the discrepancy in the parameter estimates. In conclusions, the message is double. If the final flow model misfit cannot be explained by the measurement errors, modeling errors may prevent the processes to be adequately represented. Geophysics should then be used to refine the conceptual model. On the contrary, if a priori information reveals that no model error exists, estimation of the data error (i.e., error model) should be performed accurately. This should guarantee accurate simulated results.

In the future, long-term calibration processes based on ERT-derived properties may be considered in the same way as those based on historic/punctual hydrogeological data. More importantly, in the context of climate change, such processes should be viewed as an opportunity to collect data during a natural event (sea level rise) that should occur on the time scale of human lifetimes. However, long-period calibration

processes should take into account practical problems like logistics, equipment degradation, measurement errors, dynamic boundary conditions and changes in intrinsic properties of rocks and groundwater.

Our efforts are currently focused on coupling the forward hydrological and geophysical models; this study has shown that electrical imaging data should be used for improved SWI model calibration, and thereby more reliable scenario prediction, for the sustainable management and monitoring of groundwater quantity and quality in coastal regions.

Acknowledgments
This work was partly funded by the EU project ALERT (GOCE-CT-2004-505329) and was supported by the University of Liège. We would like to thank deeply the Editor Harihar Rajaram and the Associate Editor A. Binley for motivating us in communicating the findings better since the first version of the manuscript. We thank R. de Franco and two anonymous reviewers for their constructive remarks leading to a greatly improved manuscript.

References

Abarca, E. (2006), Seawater intrusion in complex geological environments, PhD thesis, Dep. of Geotech. Eng. and Geo-Sci., Tech. Univ. of Catalonia, Catalonia, Spain.

Archie, G. E. (1942), The electrical resistivity log as an aid in determining some reservoir characteristics, *Trans. Am. Inst. Min. Metall. Pet. Eng.*, *146*, 54–61.

Barnabé, Y., U. Mok, and B. Evans (2003), Permeability-porosity relationships in rocks subjected to various evolution processes, *Pure Appl. Geophys.*, *160*(5-6), 937–960, doi:10.1007/PL00012574.

Bear, J., A. Cheng, S. Sorek, D. Ouazar, and I. Herrera (Eds) (1999), Seawater intrusion in coastal aquifers—Concepts, methods and practices, in *Theory and Applications of Transport in Porous Media*, vol. 14, Kluwer Acad., Dordrecht, Netherlands.

Binley, A., G. Cassiani, R. Middleton, and P. Winship (2002), Vadoze zone flow model parameterization using cross-borehole radar and resistivity imaging, *J. Hydrol.*, *267*(7), 147–159.

Carrera, J., A. Alcolea, A. Medina, J. Hidalgo, and L. Slooten (2005), Inverse problem in hydrogeology, *Hydrogeol. J.*, *13*(1), 206–222, doi: 10.1007/s10040-004-0404-7.

Carrera, J., J. J. Hidalgo, and E. Vazquez-Sune (2009), Computational and conceptual issues in the calibration of seawater intrusion models, *Hydrogeol. J.*, *18*(1), 131–145, doi:10.1007/s10040-009-0524-1.

Cassiani, G., G. Bohm, A. Vesnaver, and R. Nicolich (1998), A geostatistical framework for incorporating seismic tomography auxiliary data into hydraulic conductivity estimation, *J. Hydrol.*, *29*(1-2), 58–74, doi:10.1016/S0022-1694(98)00084-5.

Caterina, D., J. Beaujean, T. Robert, and F. Nguyen (2013), Comparison of image appraisal tools for electrical resistivity tomography, *Near Surf. Geophys.*, *11*(6), 639–657, doi:10.3997/1873-0604.2013022.

Cheng, A. H.-D., and D. Ouazar (Eds.) (2004), *Coastal Aquifer Management: Monitoring, Modeling, and Case Studies*, 296 pp., CRC Press, Boca Raton, Fla.

Compte, J.-C., and O. Banton (2007), Cross-validation of geo-electrical and hydrological models to evaluate seawater intrusion in coastal aquifers, *Geophys. Res. Lett.*, *34*, L10402, doi:10.1029/2007GL029981.

Dagan, G. (2006), Transverse mixing at fresh-water salt-water interfaces: An unresolved issue, paper presented at the 1st SWIM-SWICA—First International Joint Salt Water Intrusion Conference (19th Saltwater Intrusion Meeting/3rd Saltwater Intrusion in Coastal Aquifers), Automated time-Lapse Electrical Resistivity Tomography (ALERT), Cagliari, Italy.

Dahlin, T., and B. Zhou (2004), A numerical comparison of 2D resistivity imaging with ten electrode arrays, *Geophys. Prospect.*, *52*, 379–398.

Day-Lewis, F. D., K. Singha, and A. Binley (2005), Applying petrophysical models to radar travel time and electrical resistivity tomograms: Resolution-dependent limitations, *J. Geophys. Res.*, *110*, B08206, doi:10.1029/2004JB003569.

Doherty, J. (2004), *PEST: Model-Independent Parameter Estimation. User Manual*, 5th ed., 336 pp., Watermark Numerical Computing, Brisbane, Australia.

Ferré, F., L. Bentley, A. Binley, N. Linde, A. Kemna, K. Singha, K. Holliger, J. A. Huisman, and B. Minsley (2009), Critical steps for the continuing advancement of hydrogeophysics, *Eos Trans. AGU*, *90*(23), 200, doi:10.1029/2009EO230004.

Goldman, M., and U. Kafri (2006), Hydrogeophysical applications in coastal aquifers, in *Applied Hydrogeophysics*, edited by H. Vereecken et al., pp. 233–254, Springer, Netherlands.

Guhl, F., A. Pulido-Bosch, P. Pulido-Leboeuf, J. Gisbert, F. Sanchez-Martos, and A. Vallejos (2006), Geometry and dynamics of the freshwater-seawater interface in a coastal aquifer in southern Spain, *Hydrol. Sci. J.*, *51*(3), 543–555.

Gupta, S. K. (2010), *Modern Hydrology and Sustainable Water Development*, 464 pp., John Wiley. & Sons Ltd, Chichester, West Sussex, U. K.

Hayley, K., L. R. Bentley and A. Pidlisecky (2010), Compensating for temperature variations in time-lapse electrical resistivity difference imaging, *Geophysics*, *75*(4), WA51–WA59, doi:10.1190/1.3478208.

Henderson, R. D., F. D. Day-Lewis, E. Abarca, C. F. Harvey, H. N. Karam, L. Liu and J. W. Lane Jr. (2010), Marine electrical resistivity imaging of submarine groundwater discharge: Sensitivity analysis and application in Waquoit Bay, Massachusetts, USA, *Hydrogeol. J.*, *18*, 173–185, doi:10.1007/s10040-009-0498-z.

Herckenrath, D., N. Odlum, V. Nenna, R. Knight, E. Auken, and P. Bauer-Gottwein (2012), Calibrating a salt water intrusion model with time-domain electromagnetic data, *Ground Water*, *51*(3), 385–397, doi:10.1111/j.1745-6584.2012.00974.x.

Hermans, T., A. Vandenbohede, L. Lebbe, R. Martin, A. Kemna, J. Beaujean and F. Nguyen (2012), Imaging artificial salt water infiltration using electrical resistivity tomography constrained by geostatistical data, *J. Hydrol.*, *438–439*, 168–180, doi:10.1016/j.jhydrol.2012.03.021.

Hill, M. C., and C. R. Tiedeman (Eds.) (2007), *Effective Groundwater Model Calibration: With Analysis of Data, Sensitivities, Predictions, and Uncertainty*, 404 pp., John Wiley, Hoboken, N. J.

Hughes, J. D., J. T. White, and C. D. Langevin (2010), Use of time series and harmonic constituents of tidal propagation to enhance estimation of coastal aquifer heterogeneity, paper presented at the SWIM21—21st Salt Water Intrusion Meeting, Ponta Delgada, Portugal.

Huntley, D. (1986), Relations between permeability and electrical resistivity in granular aquifers, *Ground Water*, *24*(4), 466–474, doi:10.1111/j.1745-6584.1986.tb01025.x.

Huyakorn, P. S., P. F. Andersen, J. W. Mercer, and H. O. White Jr. (1987), Saltwater intrusion in aquifers: Development and testing of a three-dimensional finite element model, *Water Resour. Res.*, *23*(2), 293–312.

Kemna, A. (2000), Tomographic inversion of complex resistivity: Theory and application, PhD thesis, Ruhr-Univ., Bochum, Germany.

Koukadaki, M., G. Karatzas, M. Papadopoulou, and A. Vafidis (2007), Identification of the saline zone in a coastal aquifer using electrical tomography data and simulation, *J. Water Resour. Manage.*, *21*(11), 1881–1898, doi:10.1007/s11269-006-9135-y.

LaBrecque, D., M. Miletto, W. Daily, A. Ramirez, and E. Owen (1996), The effects of noise on Occam's inversion of resistivity tomography data, *Geophysics*, *61*(2), 538–548, doi:10.1190/1.1443980.

Lebbe, L. (1999), Parameter identification in fresh-saltwater flow based on borehole resistivities and freshwater head data, *Adv. Water Resour.*, *22*(8), 791–806.
Linde, N., A. Binley, A. Tryggvason, L. B. Pedersen, and A. Revil (2006), Improved hydrogeophysical characterization using joint inversion of cross-hole electrical resistance and ground-penetrating radar travel time data, *Water Resour. Res.*, *42*, W12404, doi:10.1029/2006WR005131.
Mallants, D., A. Espino, M. Van Hoorick, J. Feyen, N. Vandenberghe, and W. Loy (1999), Dispersivity estimates from a tracer experiment in a sandy aquifer, *Ground Water*, *38*(2), 304–310, doi:10.1111/j.1745-6584.2000.tb00341.x.
Michael, H. A., A. E. Mulligan, and C. F. Harvey (2005), Seasonal oscillations in water exchange between aquifers and the coastal ocean, *Nature*, *436*, 1145–1148, doi:10.1038/nature03935.
Morrow, F. J., M. R. Ingham, and J. A. McConchie (2010), Monitoring of tidal influences on the saline interface using resistivity traversing and cross-borehole resistivity tomography, *J. Hydrol.*, *389*(1-2), 69–77, doi:10.1016/j.jhydrol.2010.05.022.
Nguyen, F., A. Kemna, A. Antonsson, P. Engesgaard, O. Kuras, R. Ogilvy, J. Gisbert, S. Jorreto, and A. Pulido-Bosch (2009), Characterization of seawater intrusion using 2D electrical imaging, *Near Surf. Geophys.*, *7*(5-6), 377–390, doi:10.3997/1873-0604.2009025.
Ogilvy, R. D., et al. (2009), Automated monitoring of coastal aquifers with electrical resistivity tomography, *Near Surf. Geophys.*, *7*(5-6), 367–375, doi:10.3997/1873-0604.2009027.
Pandit, A., C. C. El-Khazen, and S. P. Sivaramapillai (1991), Estimation of hydraulic conductivity values in a coastal aquifer, *Ground Water*, *29*(2), 175–180, doi:10.1111/j.1745-6584.1991.tb00507.x.
Poeter, E. P., M. C. Hill, E. R. Banta, S. Mehl, and S. Christensen (2005), UCODE and six other computer codes for universal sensitivity analysis, calibration, and uncertainty evaluation, U.S. Geol. Surv. Tech. Methods, 6-A11, 283 pp.
Sanz, E., and C. I. Voss (2006), Inverse modeling for seawater intrusion in coastal aquifers: Insights about parameter sensitivities, variances, correlations and estimation procedures derived from the Henry problem, *Adv. Water Resour.*, *29*, 439–457, doi:10.1016/j.advwatres.2005.05.014.
Schlumberger (1989), *Log Interpretation Principles/Applications*., Schlumberger, Sugar Land, Tex.
Schön, J. H. (2004), *Physical Properties of Rocks: Fundamentals and Principles of Petrophysics, Handbook of Geophysical Exploration*, vol. 18, Pergamon, U. K.
Shalev, E., A. Lazar, S. Wollman, S. Kington, Y. Yechieli, and H. Gvirtzman (2009), Biased monitoring of fresh water-salt water mixing zone in coastal aquifers, *Ground Water*, *47*(1), 49–56, doi:10.1111/j.1745-6584.2008.00502.x.
Shoemaker, W. B. (2004), Important observations and parameters for salt water intrusion model, *Ground Water*, *42*(6), 829–840, doi:10.1111/j.1745-6584.2004.t01-2-.x.
Sun, N. Z., M. C. Jeng, and W. W. G. Yeh (1995), A proposed geological parametrization method for parameter-identification in 3-dimensional groundwater modeling, *Water Resour. Res.*, *31*(1), 89–102.
Therrien, R., R.-G. McLaren, E.-A. Sudicky, and S. M. Panday (2010), *HydroGeoSphere: A Three-Dimensional Numerical Model Describing Fully-Integrated Subsurface and Surface Flow and Solute Transport*, 443 pp., Groundwater Simul. GroupLaval & Waterloo Univ., Waterloo, Ontario.
Van Meir, N. (2001), Density-dependent groundwater flow: Design of a parameter identification test and 3D-simulation of sea-level rise, PhD thesis, Ghent Univ., Ghent, Belgium.
Van Meir, N., and L. Lebbe (2005), Parameter identification for axi-symmetric density-dependent groundwater flow based on drawdown and concentration data, *J. Hydrol.*, *309*(1-4), 167–177, doi:10.1016/j.jhydrol.2004.11.019.
Vandenbohede, A., L. Lebbe, R. Adams, E. Cosyns, P. Durinck, and A. Zwaenepoel (2010), Hydrological study for improved nature restoration in dune ecosystems-Kleyne Vlakte case study, Belgium, *J. Environ. Manage.*, *91*(11), 2385–2395, doi:10.1016/j.jenvman.2010.06.023.
Vecchia, A. V., and R. L. Cooley (1987), Simultaneous confidence and prediction intervals for non-linear regression models with application to a groundwater flow model, *Water Resour. Res.*, *22*(2), 95–108.
Wagner, S. R., and S. M. Gorelick (1987), Optimal groundwater quality management under parameter uncertainty, *Water Resour. Res.*, *23*(7), 1162–1174.
Werner, A. D., and C. T. Simmons (2009), Impact of sea-level rise on sea water intrusion in coastal aquifers, *Ground Water*, *47*(2), 197–204, doi:10.1111/j.1745-6584.2008.00535.x.
Werner, A. D., M. Bakker, V. E. A. Post, A. Vandenbohede, C. Lu, B. Ataie-Ashtiani, C. T. Simmons, and D. A. Barry (2012), Seawater intrusion processes, investigation and management: Recent advances and future challenges, *Adv. Water Resour.*, *51*, 3–26, doi:10.1016/j.advwatres.2012.03.004.
Yechieli, Y., U. Kafri, M. Goldman, and C. I. Voss (2001), Factors controlling the configuration of the fresh-saline water interface in the Dead Sea coastal aquifers: Synthesis of TDEM surveys and numerical groundwater modeling, *Hydrogeol. J.*, *9*, 367–377, doi:10.1007/s100400100146.